# Persistent uplift of the Lazufre volcanic complex (Central Andes): New insights from PCAIM inversion of InSAR time series and GPS data

Dominique Rémy, Jean-Luc L Froger, Hugo Perfettini, Sylvain Bonvalot, Germinal Gabalda, F. Albino, Valérie Cayol, Delphine Legrand, Michel de Saint Blanquat

Dominique Rémy, Jean-Luc L Froger, Hugo Perfettini, Sylvain Bonvalot, Germinal Gabalda, et al.. Persistent uplift of the Lazufre volcanic complex (Central Andes): New insights from PCAIM inversion of InSAR time series and GPS data. Geochemistry, Geophysics, Geosystems, 2014, 15 (9), pp.3591-3611. 10.1002/2014GC005370 . hal-03025513

HAL Id: hal-03025513
https://hal.science/hal-03025513

AGU PUBLICATIONS

Geochemistry, Geophysics, Geosystems

RESEARCH ARTICLE

10.1002/2014GC005370

**Key Points:**

- InSAR and GPS analysis using PCAIM

**Correspondence to:**
D. Remy,
dominique.remy@ird.fr

**Citation:**
Remy, D., J. L. Froger, H. Perfettini, S. Bonvalot, G. Gabalda, F. Albino, V. Cayol, D. Legrand, and M. Saint Blanquat (2014), Persistent uplift of the Lazufre volcanic complex (Central Andes): New insights from PCAIM inversion of InSAR time series and GPS data, *Geochem. Geophys. Geosyst.*, *15*, doi:10.1002/2014GC005370.

Received 4 APR 2014
Accepted 28 JUL 2014
Accepted article online 31 JUL 2014

# Persistent uplift of the Lazufre volcanic complex (Central Andes): New insights from PCAIM inversion of InSAR time series and GPS data

**D. Remy[1], J. L. Froger[2], H. Perfettini[3], S. Bonvalot[1], G. Gabalda[1], F. Albino[2,4], V. Cayol[2], D. Legrand[5,6], and M. De Saint Blanquat[1]**

[1]GET/UMR 5563 (UPS, CNRS, IRD, CNES), Observatoire Midi-Pyrénées, Université P. Sabatier, Toulouse, France, [2]LMV/UMR 6524 (UBP-CNRS-IRD), Observatoire de Physique du Globe de Clermont-Ferrand, Université B. Pascal, Clermont-Ferrand, France, [3]ISTERRE/UMR 5275 (UJF, CNRS, IRD), Observatoire des Sciences de l'Univers de Grenoble, Université Joseph Fourier, Grenoble, France, [4]Now at Department of Earth Sciences, Cartography & Remote Sensing Unit, Royal Museum for Central Africa, Tervuren, Belgium, [5]Departamento de Geofísica, Universidad de Chile, Santiago, Chile, [6]Now at Instituto de Geofisica, Universidad Nacional Autónoma de México, Coyoacan, Mexico

**Abstract** We reanalyzed the surface displacements observed at the Lazufre volcanic complex in the Southern Andean Central Volcanic Zone using GPS measurements made between 2006 and 2008 and a large InSAR data set. We performed a detailed spatiotemporal analysis of the displacements using a principal component analysis inversion method (PCAIM). The PCAIM reveals a source with no significant changes in shape and dimension and with a remarkably linear strength increase over the whole period of observation (i.e., 2003–2010). Then we used a three-dimensional mixed boundary element method (MBEM) to invert the first component of surface displacement as obtained from PCAIM. We explored a continuum of geometries from a shallow elliptic crack to a deep massive truncated elliptical cone that could represent a sill or a large magma chamber, respectively. The best models indicate a large flat-topped source with a roof area between 40 and 670 km$^2$ and a depth of between 2 and 14 km below ground surface. Lastly, on the basis of the limited data available for the thermomechanical structure of the crust in the Southern Andean Central Volcanic Zone, we consider some possible scenarios to explain the spatial and temporal pattern of displacements at Lazufre.

## 1. Introduction

Igneous intrusions such as sills and plutons are major mechanisms of constructing continental crust. The formation of these large magma bodies still eludes full understanding since they are not generally accessible until long time after their emplacement, when the action of erosion and tectonics has brought them to the surface. The Lazufre Volcanic Complex in the Central Andes (Chile-Argentina border) (Figure 1) is one of the very few places on Earth where geophysical observations of a large igneous body undergoing intrusion can be made. This volcanic area, a 30 km long chain of overlapping Quaternary volcanic centers, aligned in a N15°E direction between Lastarria (25°10′S, 68°31′W, 5706 m) and Cerro Bayo (25°24′S, 68°35′W, 5401 m) volcanoes, has attracted scientist's attention in recent years because it is one of the largest deforming volcano systems on Earth. Based on seven ERS interferograms acquired between 1995 and 2000, *Pritchard and Simons* [2002] presented the first evidence of a large-wavelength surface displacement affecting the Lazufre Volcanic Complex. The displacements are assumed to have started sometime between 1996 and 1998 (the temporal resolution of the used ERS data set did not allow Pritchard and Simons to be more precise about the displacements onset). Around this time, a large-wavelength inflation covered an elliptical area with a 30 km NNE-SSW major axis, a 25 km minor axis and a maximum displacement observed at the center of the surface displacement pattern of about 1 cm yr$^{-1}$. Using ASAR-ENVISAT Interferometric Synthetic Aperture Radar (InSAR) data collected over the same area between March 2003 and April 2005, *Froger et al*. [2007] showed the persistence of the large-wavelength inflation and detected for the first time a small wavelength deformation roughly centered beneath Lastarria volcano. Moreover, these more recent InSAR measurements revealed an apparent expansion of the area affected by surface displacement with the major axis reaching 50 km NNE-SSW and the minor axis 40 km. They also revealed an increasing of uplift rate up to

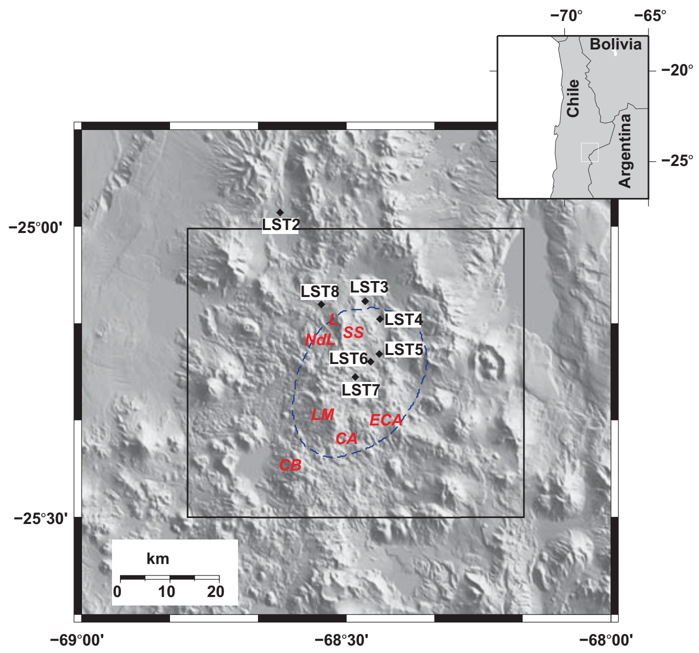

**Figure 1.** Reference map of the study area in northern Chile corresponding to the white box in the top right-hand inset map. The black square in the main map shows the area used in next figures. The black diamonds and their associated name show the location of the GPS stations. GPS data were acquired during three field surveys in November 2006, November 2007, and March 2008. The blue dashed line encircles the region which has undergone uplift over the last 7 years, as observed by InSAR in descending track 282. CA, Cordon del Azufre; CB, Cerro Bayo; ECA, East Cordon del Azufre; L, Lastarria cone; LM, La Moyra; NdL, Negriales de Lastarria; SS, South Spur.

3 cm yr$^{-1}$ in the satellite line of sight (LOS) direction; over 3 times faster than the previously observed inflation rate. The same deformation behavior and displacement rate was also reported by subsequent studies [*Ruch et al*., 2008; *Anderssohn et al*., 2009; *Ruch et al*., 2009; *Henderson and Pritchard*, 2013; *Pearse and Lundgren*, 2013]. Several lines of evidences point to this ongoing uplift being related to the presence of a large quantity of magma within the crust. Numerical modeling carried out from the InSAR data [*Pritchard and Simons*, 2004; *Froger et al*., 2007; *Ruch et al*., 2008; *Anderssohn et al*., 2009; *Henderson and Pritchard*, 2013; *Pearse and Lundgren*, 2013] all tend toward the same assumption of a large magma body located in the upper crust between 7 and 18 km below the topographic surface. Chemical and isotopic analysis of hot fluids emitted from four fumarolic areas located at the Lastarria cone suggests that the fluids originate mainly from a large, actively degassing magmatic source, with relatively recent emplacement of magmatic fluids [*Aguilera et al*., 2012]. The presence of a crustal-scale electrical conductivity anomaly beneath Lazufre has been revealed by *Budach et al*. [2013], interpreted by them as imaging partial melt rising from the upper mantle and feeding an intracrustal magma reservoir.

Despite this first-order agreement on the nature of the displacement source, several issues are unresolved, notably the shape, dimensions, and dynamics of the magmatic body as well as the precise nature of the process responsible for the uplift. *Pritchard and Simons* [2002] and *Froger et al*. [2007] proposed the presence of a magma chamber inflating at depth to explain this large-wavelength ground inflation, and they explored a large range of possible source geometries (e.g., spherical, prolate ellipsoid, and penny-shaped crack). *Ruch et al*. [2008] and *Anderssohn et al*. [2009] proposed that the uplift observed during the 2003–2008 period was caused by a fast lateral expansion, up to 8 km yr$^{-1}$, of a thin magmatic sill.

This present paper aims to perform a more rigorous investigation of the geometry of the Lazufre surface displacement source and its time-dependent behavior based on new satellite and geodetic data. We produced a database of about 550 interferograms from ascending and descending ASAR images acquired between 2003 and 2010. These data were combined to determine the vertical and easting components of the displacement field, and the results were then compared with data from GPS observations acquired during three field surveys carried out between 2006 and 2008. To invert the large time series of InSAR images and GPS data and better analyze the time-dependent behavior of surface displacement, we use the principal component analysis inversion method (PCAIM, http://www.tectonics.caltech.edu/resources/pcaim/) [*Kositsky and Avouac*, 2010; *Lin et al*., 2010; *Perfettini et al*., 2010]. This analysis of long InSAR time series and GPS data provides results which are important for the understanding of the ongoing process. It enables us to eliminate certain models as candidate for the source of the surface displacement and to discard some of the hypothesis previously invoked to explain the observed uplift at the Lazufre volcanic complex.

**Table 1.** Temporal GPS Changes Measured Between March 2006 and November 2007 and Between March 2006 and November 2008[a]

| | Location | | Displacements (2006–2007) | | | Displacements (2006–2008) | | |
|---|---|---|---|---|---|---|---|---|
| Site | Longitude (°) | Latitude (°) | East | North | Up | East | North | Up |
| LST2 | −68.625 | −24.976 | | | | | | |
| LST3 | −68.464 | −25.129 | −0.65 | 1.45 | 2.70 | −0.45 | 0.90 | 4.10 |
| LST4 | −68.437 | −25.160 | −1.50 | 2.40 | 1.20 | −0.25 | 2.45 | 2.95 |
| LST5 | −68.438 | −25.220 | −0.95 | 1.30 | 2.10 | −0.20 | 1.00 | 5.65 |
| LST6 | −68.454 | −25.233 | −0.15 | 1.10 | 6.45 | 0.15 | 1.60 | 7.45 |
| LST7 | −68.483 | −25.259 | 1.15 | 0.20 | 7.50 | 0.40 | −1.00 | 10.10 |
| LST8 | −68.547 | 25.134 | −1.70 | 1.90 | −0.25 | −1.20 | 1.00 | −0.50 |

[a] The changes are given with respect to reference station LST2. The final $1\sigma$ accuracy is estimated at 5 and 10 mm for horizontal and vertical components, respectively. The station LST7 located near the area of maximum uplift observed by InSAR indicates a ground uplift rate of about 3.85 cm ± 0.5 cm $yr^{-1}$. Depending on the station, the observation time for GPS measurements spanned between 8 days and 24–48 h (LST5 and LST6 stations) due to complex field conditions. LST2 used as reference station for both 2006 and 2008 campaigns was observed 5 and 16 days. All displacements are expressed in cm.

## 2. Data

### 2.1. GPS Data

Differential GPS measurements have been carried out on the Lazufre volcanic complex over three field trips in May 2006, November 2007, and November 2008 in order to improve constraints on the horizontal and vertical components of the surface displacement [*Bonvalot et al*., 2008]. The GPS network was composed of seven stations lying on a transect crossing the uplifting area, as delineated by previous InSAR studies [*Pritchard and Simons*, 2002; *Froger et al*., 2007; *Ruch et al*., 2008; *Anderssohn et al*., 2009; *Henderson and Pritchard*, 2013; *Pearse and Lundgren*, 2013] (Figure 1). The LST2 station was located outside the deforming area to be used as a stable reference in further network adjustments. The LST7 station is located near the center of the area affected by displacements. The GPS observations acquired using dual-frequency receivers (sessions mostly lasting from 24 to 48 h) have been processed and adjusted using GAMIT/GLOBK 10.35 software [*Herring et al*., 2010]. The final $1\sigma$ accuracy is estimated to be 5 and 10 mm for horizontal and vertical components, respectively. The resulting GPS displacements observed between May 2006 and November 2008 are shown in Table 1. These ground measurements confirm surface uplift at a rate comparable to previously published estimates. The maximum vertical displacement was measured at LST7 station (10 cm observed over the 2.5 year period) with a ground uplift rate of 3.85 ± 0.5 cm $yr^{-1}$. Horizontal displacements are clearly smaller (mostly at the level of around a centimeter) than the vertical ones. The maximum measured northing displacement reaches 2.4 cm at station LST4. In contrast to the vertical displacements, horizontal displacements do not show a clear trend during the 2 year epoch, presumably because of the low signal-to-noise ratio throughout the short time span investigated.

### 2.2. ASAR Data

A total of 64 ASAR-ENVISAT images acquired over the study area between 2003 and 2010 were used in this study (see Table 2). Thirty images were acquired from descending orbit (track 282, swath 2) and 34 from ascending orbits (track 318, swath 2 and track 404, swath 6). From this image data set, we produced a set of about 550 interferograms spanning between 35 and 2625 days. The interferograms were generated with the DIAPASON software [©*CNES/Altamira-information*, 1996] using the two-pass method described by *Massonnet and Feigl* [1998]. The orbital and topographic contributions were modeled and removed using precise orbit data from ESA DORIS and the SRTM digital elevation model oversampled to 45 m. The SRTM digital elevation model was also used to provide a geographic framework (UTM-WGS84) for the interferograms. The interferograms were then unwrapped using the Snaphu algorithm [*Chen and Zebker*, 2002]. Due to the extreme aridity of the area, most of the interferograms exhibit an excellent coherence and the unwrapping step is easily achieved without any noticeable errors. Finally, we corrected the interferograms for residual orbital and tropospheric contributions using the approach proposed by *Froger et al*. [2007]. First, we estimated the best fitting linear ramp in space and vertical phase gradient for each interferogram. Then, using these values relative to each interferogram, we performed a global data L2 adjustment to retrieve the optimal values, and their uncertainties, relative to each single ASAR image. Finally, we used the adjusted gradient values to mitigate both contributions in each interferogram.

**Table 2.** List of the 64 Envisat ASAR Images Acquired by the ENVISAT System From Two Ascending Track Orbits (Track 318 in Swath 2 and Track 404 in Swath 6) and From One Descending Track Orbit (Track 2282 in Swath 2) Between 2003 and 2010 Over the Study Area[a]

| Descending Track<br>Track 282 (swath 2) | | Ascending Tracks<br>Track 318 (swath 2) | |
|---|---|---|---|
| Orbit | Date | Orbit | Date |
| **05346** | **09 Mar 2003** | **17907** | **03 Aug 2005** |
| 05847 | 13 Apr 2003 | 19410 | 16 Nov 2005 |
| 07851 | 31 Aug 2003 | 24921 | 06 Dec 2006 |
| 10857 | 28 Mar 2004 | 26925 | 25 Apr 2007 |
| 14364 | 28 Nov 2004 | 27426 | 30 May 2007 |
| 14865 | 02 Jan 2005 | 29931 | 21 Nov 2007 |
| 15366 | 06 Feb 2005 | 30432 | 26 Dec 2007 |
| 16368 | 17 Apr 2005 | 30933 | 30 Jan 2008 |
| 16869 | 22 May 2005 | 31434 | 05 Mar 2008 |
| 17370 | 26 Jun 2005 | 34941 | 05 Nov 2008 |
| 17871 | 31 Jul 2005 | 35442 | 10 Dec 2008 |
| 19875 | 18 Dec 2005 | 35943 | 14 Jan 2009 |
| 20877 | 26 Dec 2006 | 36444 | 18 Feb 2009 |
| 21879 | 07 May 2006 | 40953 | 30 Dec 2009 |
| 22380 | 11 Jun 2006 | 41955 | 10 Mar 2010 |
| 23883 | 24 Sep 2006 | 42456 | 14 Apr 2010 |
| 24384 | 29 Oct 2006 | | |
| 24885 | 03 Dec 2006 | Track 404 (swath 6) | |
| 26889 | 22 Apr 2007 | **19496** | **22 Nov 2005** |
| 28893 | 09 Sep 2007 | 25508 | 16 Jan 2007 |
| 29394 | 14 Oct 2007 | 27011 | 01 May 2007 |
| 30396 | 23 Dec 2007 | 27512 | 05 Jun 2007 |
| 30897 | 27 Jan 2008 | 30017 | 27 Nov 2007 |
| 31398 | 02 Mar 2008 | 30518 | 01 Jan 2008 |
| 35406 | 07 Dec 2008 | 31019 | 05 Feb 2008 |
| 36408 | 15 Feb 2009 | 31520 | 11 Mar 2008 |
| 36909 | 22 Mar 2009 | 32021 | 15 Apr 2008 |
| 37410 | 26 Apr 2009 | 35528 | 16 Dec 2008 |
| 39915 | 18 Oct 2009 | 36029 | 20 Jan 2009 |
| 42921 | 16 May 2010 | 37031 | 31 Mar 2009 |
| | | 40037 | 27 Oct 2009 |
| | | 40538 | 01 Dec 2009 |
| | | 41039 | 18 Jan 2010 |
| | | 41540 | 09 Feb 2010 |
| | | 42041 | 16 Mar 2010 |
| | | 42542 | 20 Apr 2010 |

[a] Time series reference orbit and date are indicated in bold for each track.

## 3. InSAR Time Series Analysis

In order to characterize the time dependency of displacements as accurately as possible and to reduce the inherent redundancy within the interferogram data set we used a two-steps approach. The first step was to generate a time series for each track relative to the earliest SAR image using a technique similar to the one proposed by *Usai et al.* [2003]. The second step, involved decomposing the displacement maps obtained from the first step into their principal components using the approach proposed by *Kositsky and Avouac* [2010]. The principal component decomposition allows the displacement maps to be resolved into a superposition of several components, each of them characterized by its own temporal evolution. This type of decomposition is particularly advantageous for displacement inversions in which the displacement signal can be represented by a small number of components thus considerably reducing the amount of data to be inverted.

### 3.1. Time Series Generation

The time series generation consists of a global data adjustment where the displacements relative to single images (i.e., to single acquisition times) are retrieved from differential displacements relative to the interferograms. The good temporal coherence of the study area guarantees a high proportion of usable interferograms for the time series generation (more than 60% of the interferograms with perpendicular baseline lower than 350 m). Before processing the time series, we make the phase values comparable in both space and time by selecting a reference point outside of the area affected by displacements and by correcting each interferogram for a constant shift calculated as the mean phase value of a $2.8 \times 2.8$ km window centered on the reference point.

Figure 2 shows some adjusted LOS displacement maps spanning different time intervals during the 2003–2010 period. These maps exhibit a conspicuous large-wavelength elliptical displacement pattern that corresponds in location to the large uplift already described in previous studies [*Pritchard and Simons*, 2002; *Froger et al.*, 2007; *Ruch et al.*, 2008; *Anderssohn et al.*, 2009; *Henderson and Pritchard*, 2013; *Pearse and Lundgren*, 2013]. When considering the whole time series, the extent and amplitude of the displacement pattern increases as a function of time. However, the major axis/minor axis ratio of the pattern remains remarkably constant, with a value close to 5/4. This suggests that the shape of the surface displacement source does not change significantly throughout the entire studied period. The LOS velocity maxima at the center of the displacement pattern for the track 282, 318, and 404 are estimated to be: $-3$, $-3.2$, and $-2.75$ cm yr$^{-1}$ toward the satellite. The value estimated for track 282 is in agreement with those given in

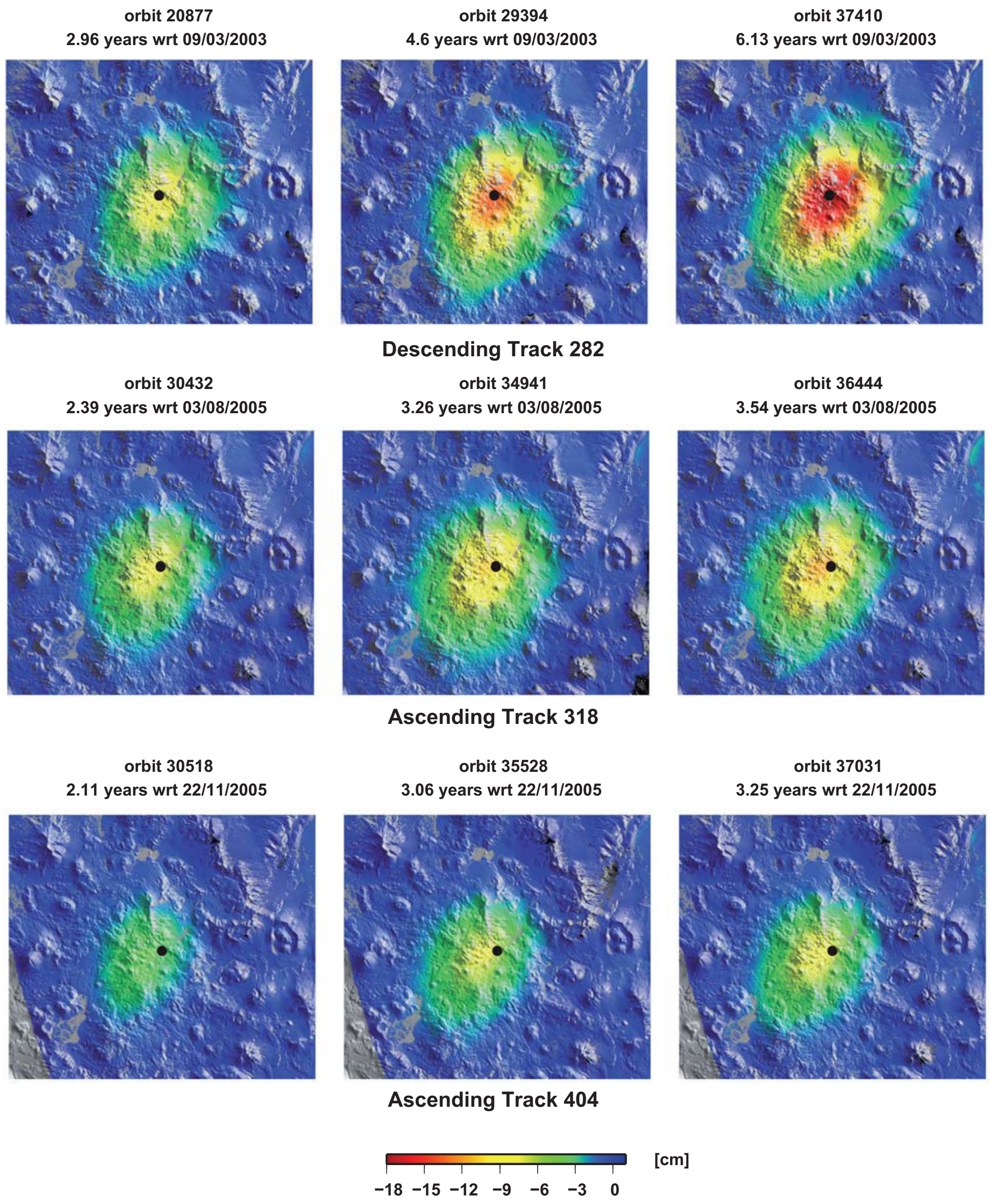

**Figure 2.** Adjusted LOS displacement maps overlaid onto a shaded relief map. (a) Descending track 282 (swath 2) displacement maps from March 2003 to February 2006, October 2007, and April 2009, respectively. (b) Ascending track 318 (swath 2) displacement maps from August 2005 to December 2007, November 2008, and February 2009. (c) Ascending track 404 (swath 6) displacement maps from November 2005 to January 2008, December 2008, and March 2009. Displacements toward the satellite are negative. The black circle shows the location of the GPS station LST7. The differences in deformation pattern between the three sets of images are due to the difference in viewing geometry.

previous studies [*Froger et al.*, 2007; *Ruch et al.*, 2008; *Anderssohn et al.*, 2009; *Henderson and Pritchard*, 2013; *Pearse and Lundgren*, 2013].

### 3.2. PCAIM Decomposition

The principal component analysis-based inversion method (PCAIM) relies on principal component analysis of the surface displacement time series. In this approach, the displacement data are decomposed into a linear combination of principal components. Each component is associated with its own spatial vector, singular value, and time function, where the singular value is a measure of the significance of the component. PCAIM makes it possible to handle large and heterogeneous data sets, unevenly distributed in time, such as those obtained by combining multitrack InSAR data and GPS measurements. Furthermore, contrary to classical principal component decomposition, it makes it possible to take the data uncertainties properly into account. In favorable cases, PCAIM can provide a decomposition of the data set into only a few components. It is then clearly advantageous, in term of computing time, to invert these few components rather than the entire data set in order to obtain simultaneously the displacements source characteristics for all the epochs. The main principle of the method is presented in the work of *Kositsky and Avouac* [2010] or in the PCAIM manual and examples of applications can be found in the works of *Lin et al.* [2010] and *Perfettini et al.* [2010].

To reduce the computational cost of the principal component decomposition, we subsampled each displacement map on a 500 m uniform grid. This simple way to break down the data is suitable in our case in which the displacement signal is a smooth and large-wavelength signal. It allows the number of data to be reduced by about two orders of magnitude without losing many details of the displacement.

Our resulting subsampled InSAR time series consists of 30 epochs on 14,561 observations, 16 epochs on 14,535 observations, 18 epochs on 14,116 observations for the track 282, 318, and 404, respectively, giving a total of $9.2 \times 10^5$ InSAR measurements. The three InSAR time series are combined into a large displacement data matrix $\boldsymbol{X}$ of 43,212 lines (total number of subsampled measurements multiplied by the number of tracks) and 64 rows (the total number of epochs). For each time series, we interpolated the displacement values and errors at the missing epochs over the period spanned by the time series and we extrapolated displacement values, assigning an infinite error for missing epochs outside the period spanned by the time series. The InSAR data are weighted either inversely proportional to the estimated variance or at zero for extrapolated missing values.

The N × M data matrix $\mathbf{X}$ is first centered such that the time series $\overline{\boldsymbol{X}}=\boldsymbol{X}-\langle\boldsymbol{X}\rangle$ has a mean value of zero. Next PCAIM decomposes $\overline{\boldsymbol{X}}$ into the sum of its principal components:

$$\overline{\boldsymbol{X}} = \boldsymbol{U}.\boldsymbol{S}.\boldsymbol{V}^{\tau} \tag{1}$$

where $\boldsymbol{U}$, $\boldsymbol{S}$, and $\boldsymbol{V}$ have a size of N × N, N × M, and M × M, respectively, and $^{\tau}$ means that the matrix is transposed. $\boldsymbol{U}$ is the spatial functions matrix where the lines correspond to the subsampled data and the columns to the principal components, and it is only space dependent (N × N matrix). $\boldsymbol{S}$ is the matrix of the principal values, a diagonal matrix with r nonzero eigenvalues (i.e., r is the S matrix rank) that gives the magnitude of each component. $\boldsymbol{V}$ is the time function matrix as it is solely time dependant (M × M matrix).

Figure 3 summarizes the results obtained from the PCAIM decomposition of our InSAR time series. In Figure 3a, we show the normalized singular values for each component. It is noteworthy that the first component has a singular value one order of magnitude larger than that of the second component. This is clear evidence that most of the InSAR data information is contained in the first principal component. This is confirmed by the spatial functions for the first principal component for the three tracks (Figure 3b) that remarkably mimics the displacement pattern observed on the time series. In comparison, the spatial functions of the second and third principal components are quite noisy. The time function for the first principal component (Figure 3c) appears remarkably linear, a feature in good accordance with the results previously obtained from the analysis of the ground inflation signal observed during several periods from 2003 to 2010 [*Froger et al.*, 2007; *Ruch et al.*, 2008; *Anderssohn et al.*, 2009; *Henderson and Pritchard*, 2013; *Pearse and Lundgren*, 2013]. Time functions for second and third components show signs of transient signals which we attributed to tropospheric effects.

In order to determine how the data are represented by the components, we computed the reduced Chi-square $\chi_r^2$ of the residual to the data for the 1 to kth components using the following formulation [*Lin et al.*, 2010]:

$$\chi_r^2 = \frac{1}{N-k} \sum \left[ \frac{\boldsymbol{X}-\boldsymbol{X}_{\boldsymbol{svd}}}{\sigma} \right]^2 \tag{2}$$

where $N$ refers to the number of subsampled InSAR data, $k$ is the number of principal components selected for the signal reconstruction, $\boldsymbol{X}$ is the subsampled InSAR data matrix, $\boldsymbol{X}_{\boldsymbol{svd}}$ is the reconstructed data matrix

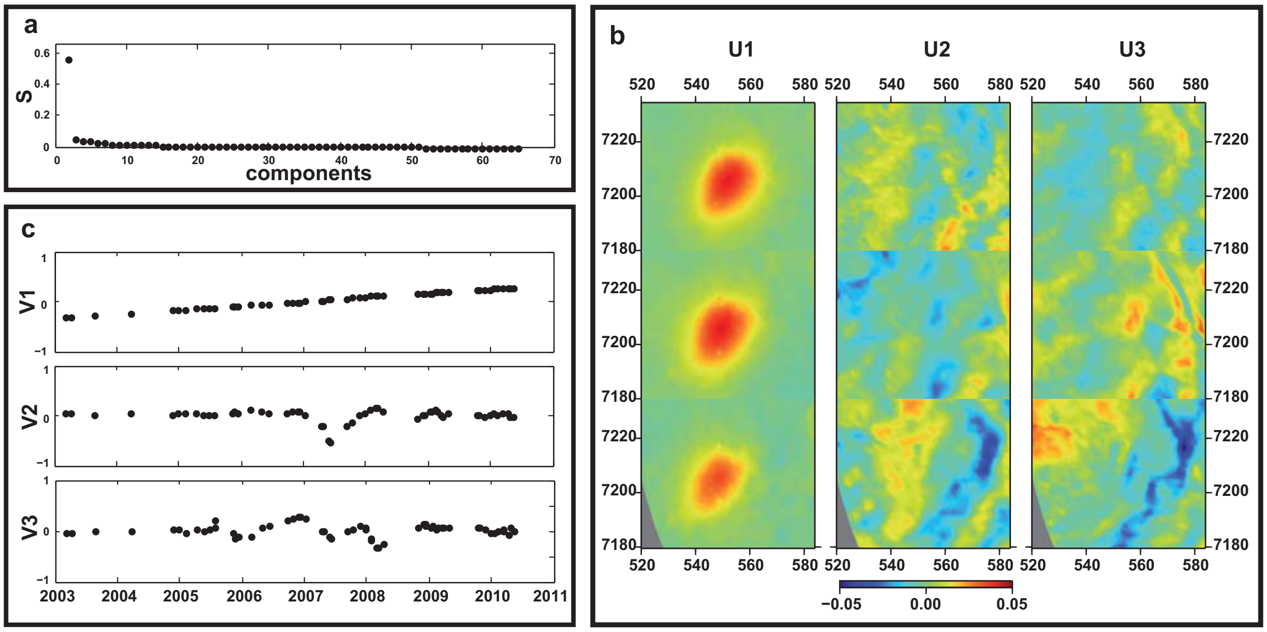

**Figure 3.** Results from the PCA decomposition applied to the InSAR time series. (a) Diagonal of the matrix of the normalized principal values. In this figure, the principal values are divided by the sum of the principal values. The proportions of variation explained by the first and the second principal values are 0.6 and 0.07, respectively. The linear combination of the first principal component using U1, S1, and V1 reconstructs the observed signal within the 5 mm uncertainty ($\chi_r^2$ of 0.3). (b) The three first spatial functions of the displacement field for swath 2282, 2318, and 6404 from top to bottom. The first spatial function shows that the signal is clearly related to inflation, as observed with different look angles (swaths 2 and 4) and different heading angles (ascending and descending). (c) Three first time functions. The first time function evolves linearly with time and is related to the temporal evolution of the ground inflation signal observed during the 2003–2010 period. Some of the topography-related atmospheric signal is also mixed into the first spatial function. Higher principal components are quite noisy and show signs of transient signals that can be attributed to short-timescale tropospheric effects. The area shown in gray corresponds to a region which is not covered by track 604. The lack of appearance of the pattern related to the small deformation source beneath Lastarria cone is due to the downsampling of the InSAR data to 500 m pixel.

obtained by multiplying the first spatial components of $k$ by their singular values and by their time functions, and $\sigma$ is the InSAR data standard error estimated to 5 mm. The interpolated missing epochs are not considered in the estimation of the $\chi_r^2$.

If the signal is correctly reconstructed for a component then the Chi-square value is expected to be close to 1; otherwise the uncertainty of the measurements are either over or underestimated. The $\chi_r^2$ of the residuals between the observed and the reconstructed time series for the first to the eighth component ranges from 0.25 to 0.003. These values lower than 1 indicate that the residuals between data and the reconstructed time series lie within the data uncertainty whatever the number of components used, thus the data can be sufficiently well estimated by the first component alone. The Chi-square value of 0.25 obtained for the residual between the data and the first component might indicate that our estimation of the InSAR data uncertainty of 5 mm is overestimated but this would be misleading. Figure 4 shows an example of six selected observed and reconstructed LOS displacement maps using the first principal component for the decomposition. Visual inspection of these maps reveals the presence of topography-related atmospheric effects in spite of the correction made during the construction of interferograms. The first spatial function is partially biased by these effects because they are coherent in space and, due to the uneven sampling of SAR data, they could also appear coherent in time. Consequently, the topography-related atmospheric effects are decomposed into the sum of a first component, which reproduces the linear behavior of the signal, and the high-order components which reproduce the deviation from this linear trend. However, thanks to the correction made during the interferogram processing, the residual of topography-related atmospheric effects are weak and barely affect the decomposition.

Taking these results into account, we considered that the contribution of higher order components was negligible and likely within the data noise. Thus, we decided to retain only the first component to reconstruct the original data. Generally, each individual principal component represents a linear combination of the contribution from various sources rather than one particular identifiable physical source. Here, however, the signal can be described using the first component alone and a good approximation of $\overline{\boldsymbol{X}}$ could be:

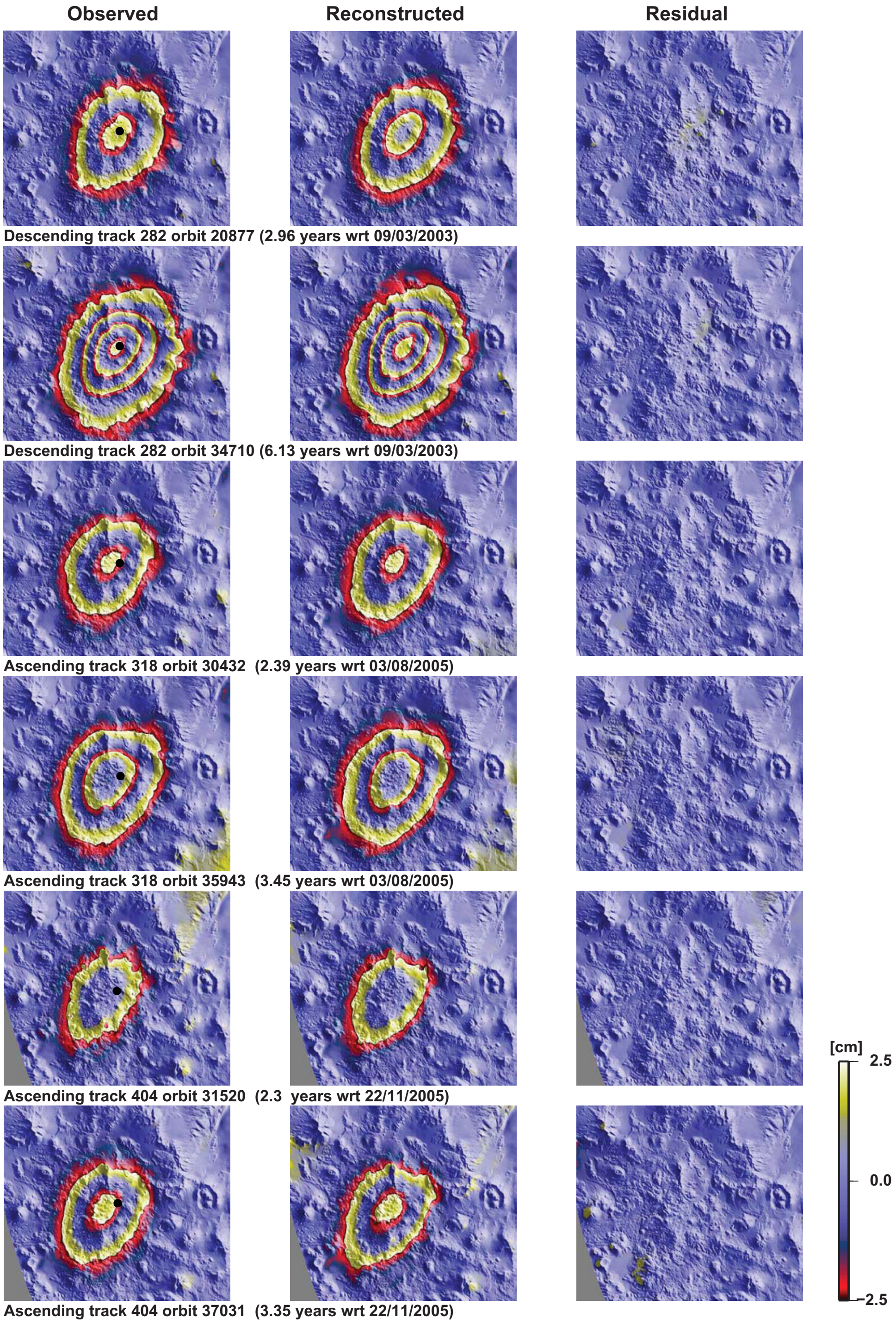

**Figure 4.** Example of several reconstructed adjusted LOS displacement maps using the first principal component of the PCA decomposition. (left) Adjusted LOS displacement maps using the InSAR data subsampled to 500 m. (middle) Reconstructed adjusted LOS displacements maps using the first component. (right) Residual of the difference between observed and reconstructed displacements. The root mean square between observed and reconstructed data ranges from 2 to 2.5 mm. All the images are shown with a 5 cm color cycle. Visual inspection of the displacements maps reveals the presence of residual topography-related atmospheric effects in spite of the corrections made during the construction of the interferograms. These effects partially bias the first spatial function but barely affect the decomposition. The black circles show the location of the GPS station LST7.

**Table 3.** Comparison of GPS and InSAR Data[a]

| | Descending Track 282 | | | | Ascending Track 318 | | | | Ascending Track 404 | | | |
|---|---|---|---|---|---|---|---|---|---|---|---|---|
| | 2006–2007 | | 2006–2008 | | 2006–2007 | | 2006–2008 | | 2006–2007 | | 2006–2008 | |
| Name | InSAR | GPS | InSAR | GPS | InSAR | GPS | InSAR | GPS | InSAR | GPS | InSAR | GPS |
| LST2 | 0.00 | 0.00 | −0.00 | 0.00 | −0.35 | 0.00 | −0.45 | 0.00 | −0.25 | 0.00 | −0.10 | 0.00 |
| LST3 | −2.35 | −3.30 | −3.00 | −4.70 | −1.40 | −2.90 | −2.00 | −4.10 | −0.75 | −2.35 | −1.10 | −3.30 |
| LST4 | −4.15 | −2.40 | −5.25 | −4.50 | −2.20 | −2.00 | −3.10 | −3.10 | −1.20 | −1.80 | −1.65 | −2.30 |
| LST5 | −10.25 | −7.85 | −12.90 | −10.40 | −4.95 | −3.15 | −7.10 | −6.10 | −2.45 | −1.75 | −3.90 | −4.00 |
| LST6 | −12.20 | −12.20 | −15.30 | −13.20 | −6.00 | −7.3 | −8.45 | −8.05 | −3.00 | −4.40 | −4.85 | −4.85 |
| LST7 | −13.60 | −14.65 | −16.95 | −16.90 | −7.00 | −7.65 | −10.10 | −10.45 | −3.85 | −4.20 | −6.30 | −6.85 |
| LST8 | −1.20 | 0.50 | −1.60 | 0.45 | −1.15 | −0.20 | −1.80 | 0.10 | −0.70 | −0.40 | −1.15 | 0.10 |

[a] We list the values of displacement projected in the LOS direction for GPS data acquired during three field surveys carried out in March 2006, November 2007, and November 2008. The root mean square (rms) difference between LOS-projected GPS displacements and InSAR measurements is about 1.3 cm. All measurements are expressed in cm. Displacements toward the satellite are negative.

$$\overline{\boldsymbol{X}} \cong \boldsymbol{U}_1.S_1.\boldsymbol{V}_1^{\tau} \tag{3}$$

where $\boldsymbol{U}_1$ (N × 1 matrix) is the first spatial vector. $S_1$(scalar) is the first principal value, $\boldsymbol{V}_1$(M × 1 matrix) is the first time function. In this equation, only $\boldsymbol{V}_1$ evolves with time whereas $\boldsymbol{U}_1$ and $S_1$ remain constant. This result leads to the important conclusion that the shape of the displacement field does not change with time during the studied period and that only the amplitude of the signal varies over time.

### 3.3. Consistency of InSAR and GPS Measurements

An independent way to evaluate the relevance of the first principal component as an estimation for the InSAR data is by comparing it with the GPS measurements. In order to make the two sets of geodetic data comparable in time, we reconstructed the InSAR displacements at the epoch of the GPS measurements using the first principal component time function obtained from the PCAIM analysis. Then, to make the data sets geometrically comparable, we projected the GPS vectors into the respective LOS for each InSAR track.

The InSAR time series are in good agreement with the LOS-projected GPS displacements for all tracks (see Table 3). The differences between the two data sets range from 0.02 to 1.26 cm for a root mean square of about 1 cm. These differences are assumed to result mainly from orbital uncertainties, uncorrected atmospheric effects in the SAR images and the larger uncertainties in the GPS vertical determinations which are propagated into the LOS projection. Figure 5 shows, as an example, the LOS-projected GPS displacements and the InSAR reconstructed at location of LST7. The accordance between the two data sets at this station located near the area of maximum uplift clearly indicates the good consistency between the inferometric and GPS observations and confirms the relevance of using the first principal component as a proxy for the InSAR displacement time series.

## 4. Constraints on the Shape of the Displacement Source

A large range of inflating source geometries, including sphere, prolate ellipsoid, or planar crack, located between 7 and 18 km below the surface, have been proposed in previous studies to explain the displacements at Lazufre [*Pritchard and Simons*, 2004; *Froger et al.*, 2007; *Ruch et al.*, 2008; *Anderssohn et al.*, 2009; *Henderson and Pritchard*, 2013; *Pearse and Lundgren*, 2013]. This wide range of acceptable source shapes reflects the inherent nonuniqueness of inverse deformation problem, aggravated by the fact that the InSAR data, used in previous studies, were mostly acquired along a single track and thus provide weak constraints on the source geometry. *Anderssohn et al.* [2009] tried to derive two-dimensional surface displacement fields by combining descending interferograms produced from Stripmap ASAR data with one ascending interferogram produced from Wide Swath ASAR data. But, as only one Wide Swath interferogram was suitable for this purpose, the resulting displacement field was poorly constrained.

A way to reduce the range of possible solutions is to consider additional constraints on the source geometry, such as those provided by comparison of the horizontal and vertical displacement components. For

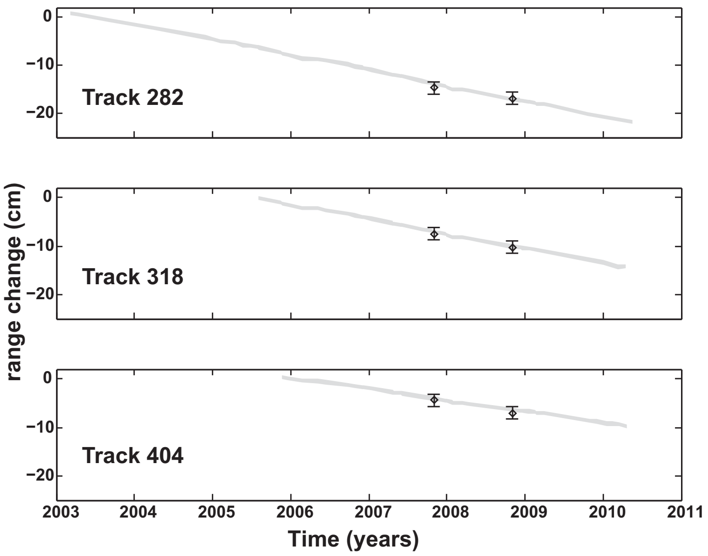

**Figure 5.** Corresponding time series of reconstructed LOS displacements and their uncertainties for tracks 282, 318, and 604, as observed at the station LST7. The diamonds are the LOS-projected GPS data observed in November 2007 and November 2008, with their standard errors.

example, it is well known that the ratio of maximum horizontal displacements to maximum vertical displacements is a good indicator of the source roof geometry [*Dieterich and Decker*, 1975; *Fialko and Pearse*, 2012]. In particular, within homogeneous elastic half-space, flat-topped sources produce lower ratios than convex-topped sources such as the spheres or prolate ellipsoids which are often used as a simplification to model magma bodies [*Dieterich and Decker*, 1975; *Fialko et al*., 2001a; *Yun et al*., 2006]. Since the InSAR data used in the present study were acquired from three independent tracks from ascending/descending passes, they theoretically allow the 3-D displacement components (easting, northing, and vertical) to be retrieved. In reality, due to the near-polar orbits of ENVISAT, the northing displacement component is poorly constrained. Therefore, we have based our analysis of the displacements only on the easting, and vertical components assuming that northing displacements are not significantly higher in magnitude than these other components and then vanish when projected in the radar line of sight. This assumption is confirmed by the values of northing displacements measured with GPS that account, on average, for about one-third of the total displacement. A prerequisite for retrieving the easting and vertical components is to have the three independent InSAR displacements compatible in time. This step is easily achieved by using the InSAR displacements reconstructed using the first principal component time function at the GPS epochs, taking the epoch of the first GPS campaign as the time reference (i.e., null displacement). Then, the easting and vertical displacement components can be obtained using the approach proposed by *Wright et al.* [2004].

The resulting horizontal and vertical displacement maps derived from InSAR data between May 2006 and November 2008 are shown in Figure 6 along with the measured GPS vectors for the same period. The vertical displacements affect an elliptical area with a 30 km NNE-SSW major axis and a 19 km minor axis. They reach up to 8.5 cm at the center of the displacement pattern. This value differs slightly from the vertical displacement measured by GPS at LST7 (10.1 cm) but the difference falls within the 95% confidence interval. The easting displacements are low and range from $-2.5$ to 2.0 cm. In addition, in Figure 6, there is a rough symmetry (respectively, antisymmetry) of the vertical (respectively, the easting) component with respect to a N15°–N40° axis, which suggests a first-order symmetry of the surface displacement source. A more careful examination of the easting displacement reveals that the displacement amplitude is lower on the east side of the uplift. This observation suggests that the source roof could not be completely horizontal. Figure 7 shows the retrieved vertical and easting displacements along an east-west profile (AA′ in Figure 6) crossing the maximum area of uplift, compared with the best computed responses derived from analytical models of displacement sources embedded in a homogeneous isotropic Poissonian elastic half-space (spherical point source, penny-shaped crack, rectangular tensile dislocation, prolate spheroid) [*Mogi*, 1958; *Yang and Davis*, 1988; *Okada*, 1992; *Fialko et al*., 2001a]. The ratio of maximum retrieved horizontal displacement to the maximum retrieved vertical displacement is about 0.3, suggesting a rather flat-topped source. This inferred flat-topped nature of the source is also consistent with the better agreement between the retrieved displacements and those modeled with the tensile dislocation than those with other analytical models (Figure 7).

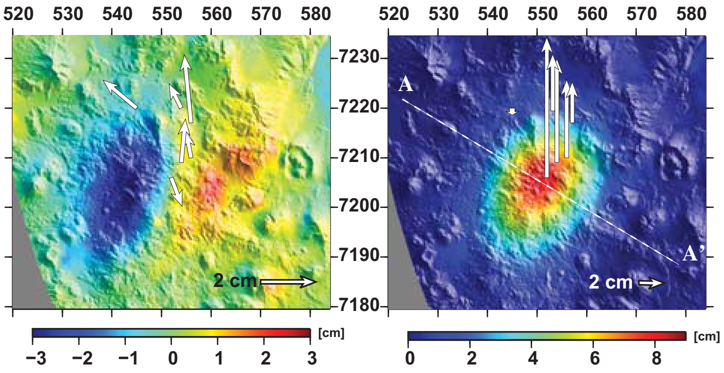

**Figure 6.** Easting and vertical components of the displacement observed between May 2006 and November 2008, determined by the combination of ascending and descending InSAR data. (left) Easting component of the ground surface displacement. Negative values indicate a displacement to the west whereas positive value indicates a displacement to the east. (right) Vertical component of the ground surface displacement. Vectors show the vertical and horizontal components observed by GPS. GPS data and the maps span the same time period. The dashed line AA′ shows the profile used in Figure 7. Note that a different color scale is used between the two maps to improve contrast between them. Coordinates are expressed in UTM-WGS84 (19 zone South). The area shown in gray corresponds to a region which is not covered by the track 604.

## 5. Modeling Strategy

The results provided by the comparison of vertical and horizontal displacements on one hand, and by the PCAIM analysis on the other hand, led us to focus our modeling investigation on a flat-topped body whose size and shape do not change over time but whose internal pressure increases. We considered two end-member models; first an elliptical crack, i.e., a model with a very low geometric aspect ratio (thickness:diameter) which represents a sill-like source; and second an elliptical truncated cone that is suitable for modeling massive sources such as large magmatic chambers or plutons. Therefore, compared to the traditional approach which consists of looking for tensile opening aligned on the same plane, our approach allows us to explore a broader range of possible source geometries.

We calculated the displacements produced by our two end-member models using a three-dimensional mixed boundary element method (BEM) for linear elastic media [*Cayol and Cornet*, 1998; *Fukushima et al.*, 2005]. This numerical modeling method can incorporate realistic topography, and any number of pressure sources with different geometries. We assumed that the sources were embedded in an isotropic homogeneous elastic half-space limited by the surface topography and that uniform pressure acted on all the source boundaries (unlike the constant displacement discontinuity models). We chose a shear modulus of 30 GPa and a Poisson's ratio of 0.25.

We performed an inversion of the InSAR and GPS data using a neighborhood search algorithm [*Sambridge*, 1999a, 1999b]. In this approach, the solution of the inverse problem is described in term of posterior probability density (PPD) functions that estimate the confidence limits on a given model and provide a full description of the correlation between the model parameters.

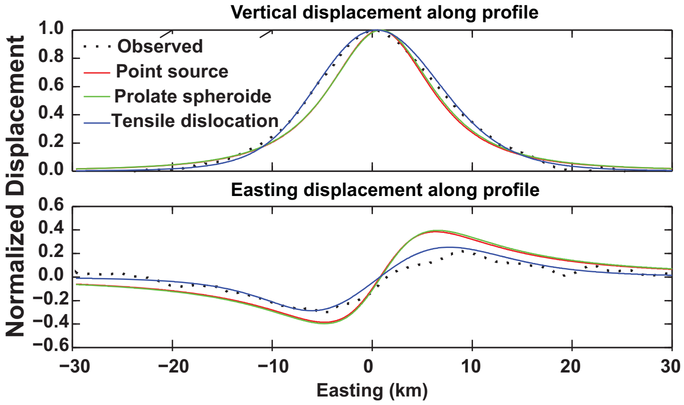

**Figure 7.** Profiles of vertical and east-west components of the ground surface displacement along AA′ (shown in Figure 6). Components determined by InSAR are shown in dot. Colored lines show displacement modeled using a prolate spheroid, a spherical point source, and a tensile dislocation. The ratio of the horizontal peak to maximum vertical displacement of 0.27, for the observed displacement, is close to the one obtained using the tensile dislocation model, suggesting that the source is a flat-topped body.

A classical approach in modeling InSAR measurements is to invert the displacement data available for each epoch. Here, however, the PCAIM approach allows the number of inversions to be reduced significantly since only the first principal component is inverted. Given that we considered the crust as a linear elastic medium (i.e., displacements are proportional to source pressure variations) we can write

$$\boldsymbol{X}=\boldsymbol{G}.\Delta\boldsymbol{P} \qquad (4)$$

**Table 4.** Elliptical Crack Model Parameters Inferred From the Inversion of the Geodetic Data[a]

| | | | 95% Confidence Intervals | | |
|---|---|---|---|---|---|
| Parameters | Minimum Values | Maximum Values | Lower | Upper | Best Values |
| X (km) | 549 | 554 | 551.050 | 553.350 | 552.310 |
| Y (km) | 7203 | 7208 | 7203.960 | 7206.420 | 7205.380 |
| Depth (m) | 1000 | 20000 | 8750 | 13,950 | 11,135 |
| S1 (m) | 5000 | 40000 | 21460 | 34,820 | 29,690 |
| S2/S1 | 0.1 | 1 | 0.1 | 0.66 | 0.43 |
| DipS1 (°) | 15°S | 15°N | 12°S | 7°N | 2.5°S |
| DipS2 (°) | 15°W | 15°E | 7°W | 13°E | 3.5°E |
| Azimuth (°) | N80°E | N | N45°E | N20°E | N34°E |
| Area ($km^3$)[b] | | | 44 | 530 | 298 |

[a] X and Y are expressed in km (UTM WGS84 zone 19 South). Depth is expressed in m below the mean surface elevation (i.e., 4500 m a.s.l). S1 is the major axis. S2/S1 is the length ratio between the major and minor axes. DipS1 and DipS2 are the dip angles of the major axis (S1) and the minor axis (S2), respectively. Azimuth is a clockwise angle relative to the North.

[b] Confidence interval and best estimation for the source area are estimated using the geometric parameters inferred by the inversion.

where $\boldsymbol{X}$ is the InSAR data matrix, $\boldsymbol{G}$ is a Green function matrix of N × 1 (N number of sampled points). $Gi_1$ represents the projected LOS displacement induced at a given pixel i due to unit pressure variation for a given displacement source model and $\Delta\boldsymbol{P}$ is a vector of 64 unknown pressure changes at each epoch.

Then, from the combination of equations (3) and (4) we can infer the pressure change history of the source

$$\Delta\boldsymbol{P} \cong \boldsymbol{P}_0 + (\boldsymbol{G}^{-1}\boldsymbol{U}_1).S_1.\boldsymbol{V}_1^{\tau} \tag{5}$$

where $\boldsymbol{P}_0 = (\boldsymbol{G}^{-1}X)$ represents the pressure that accounts for the mean displacement of each pixel. The product $\left(\boldsymbol{G}^{-1}.\boldsymbol{U}_1\right).S_1$ is only space dependent and remains constant as previously shown while $\boldsymbol{V}_1$ is only time dependant.

Next we used the following misfit function which presents a minimum for the best source inferred jointly by InSAR and GPS data:

$$\chi_m^2 = \sum_i \left( \frac{(\boldsymbol{U}_m(i) - \boldsymbol{U}_{obs}(i))}{\sigma(i)} \right)^2 \tag{6}$$

where $\boldsymbol{U}_{obs}$ and $\boldsymbol{U}_m$ represent observed and modeled displacement, respectively, and $\sigma$ the uncertainties of the observed GPS displacements and InSAR measurements.

### 5.1. Elliptical Crack Source

Our elliptical crack model involves eight parameters: coordinates of the crack center (the easting, northing, and depth), the length of the major and minor axes, the dip, and azimuth of the major axis and the dip of the minor axis. Table 4 summarizes the lower and upper bound search values for each parameter and reports the best model parameters with uncertainty level of 95% deduced from the inversion. The geographical location and the azimuth of the displacement source are well resolved as indicated by their narrow 95% confidence intervals. The dip of major and minor axes is also relatively well constrained and indicate that the source roof is close to horizontal. The depth of the best crack model ranges from 8750 to 13,950 m (95% confidence level) below ground surface. Figure 8 shows the two-dimensional posterior probability density function between the depth and the area of the elliptical crack model. The uncertainty on the depth is high due to a trade-off between this parameter and the surface area of the source. In other words, as the depth and the surface area of the source, defined by the length of the major and minor axes, both influence the wavelength of the surface displacement, there is a continuum of parameter combinations between an extensive source (e.g., ~450 $km^2$) lying at intermediate depth (e.g., ~9 km) and a small source (e.g., ~40 $km^2$) at greater depth, that equally well reproduce the observed displacement pattern (see Figure 8). Obviously, this also leads to an uncertainty in the determination of the source opening rate. For instance, we obtain maximum opening rate ranging from 5 mm $yr^{-1}$ to 50 cm $yr^{-1}$ (95% confidence level). Unfortunately, without additional information, we cannot reduce these uncertainties further.

The elliptical crack model, which matches the whole geodetic data set best, is shown in Figure 9. The reduced $\chi_m^2$ (i.e., the $\chi_m^2$ divided by the degree of freedom) of the residuals between the values predicted by

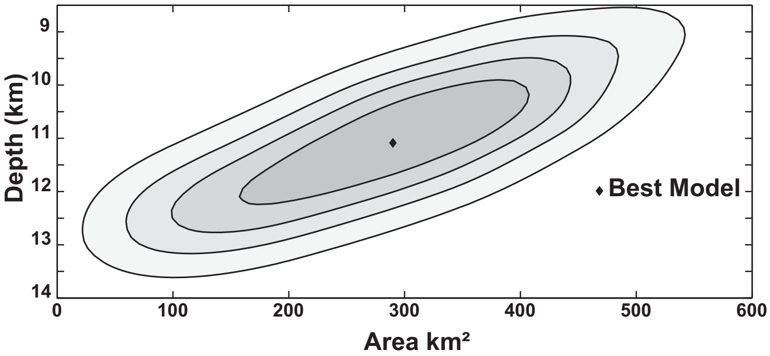

**Figure 8.** Two-dimensional marginal posterior probability density function (PPD) between the depth and the area of the elliptical crack model. This figure highlights the trade-off between these two parameters. Contour interval is 0.2 times the maximum value. The black diamond represents the best model (reduced $\chi^2_m = 0.78$).

the model and the data is 0.78. The RMS of residuals for InSAR is about 4 mm while the corresponding RMS for the GPS is 10 mm. The surface area of the source is 298 km$^2$. In Figures 9d–9l, we compare the displacements observed on the largest period of each track to the modeled displacements and we show their residuals. For the track 2282 data, which represent more than 6 years of displacements, the maximum estimated source opening reaches up to 7.2 cm yr$^{-1}$ with an average of about 4.7 cm yr$^{-1}$, leading to a volume change rate of 14.8 $\times$ 10$^6$ m$^3$ yr$^{-1}$ and a pressure increase of 8 $\times$ 10$^{-2}$ MPa yr$^{-1}$ assuming a shear modulus of 30 GPa. This volume change estimate is close to those previously proposed by [*Pritchard and Simons*, 2004; *Froger et al*., 2007] and the value of opening rate is close to those proposed by *Ruch et al*. [2008], *Anderssohn et al*. [2009], and *Pearse and Lundgren* [2013].

### 5.2. Elliptical Truncated Cone

The elliptical truncated cone source involves 10 parameters. The shape and location of its roof are determined by the same eight parameters used for the elliptical crack source, and two additional parameters include the source thickness and the dip angle of the side walls. The root of the cone is a homothetic image of its roof giving either a cone which widens downward, or a cone which narrows downward. Table 5 summarizes the lower and the upper boundary search values for each parameter and reports the best model parameters with their uncertainties at 95% level confidence deduced from the inversion. The geographical location, the azimuth, and the dip of both major and minor axes are reasonably well constrained and their inferred values and confidence intervals are close to those inferred from the inversion of the elliptical crack model. On the contrary, the depth, thickness and dip of the source walls are poorly constrained, as these parameters can vary widely without degrading the fit to the data. The minimum depth of the source roof, at 2000 m below the ground surface, is strikingly smaller than the one obtained for the elliptical crack models (8750 m).

Figure 10 shows scatter plots of the source depth versus the dip angle of the source walls, the source thickness and the source volume deduced from the S1, S2, and thickness parameters using all the computed solutions that fall within the 95% confidence interval. These scatter plots reveal that the dip angle of the walls, the thickness, and the induced volume of the source are highly correlated with the depth and, hence poorly determined.

Shallow sources (depth $<$ 8000 m) are characterized by a large volume ($>$400 km$^3$, Figure 10c) and by outward dipping sides. For sources with a depth greater than 8500 m the ground surface displacements are mainly determined by the thickness and the depth of the source but are completely insensitive to dip angle of the walls. As a consequence, the surface displacements are also insensitive to the dimensions of the source root. This finding is in agreement with *Yun et al*. [2006] who showed that if the radius of a flat-topped source is large compared to its depth, then the ground surface displacements are dominated by displacement of the source's upper surface.

Although deep sources ($z > 8500$ m) could have a good $\chi^2$, our inversion tends to favor a large shallow source (27 and 15 km for the major and minor axes) lying at 5 km depth with its walls dipping outward

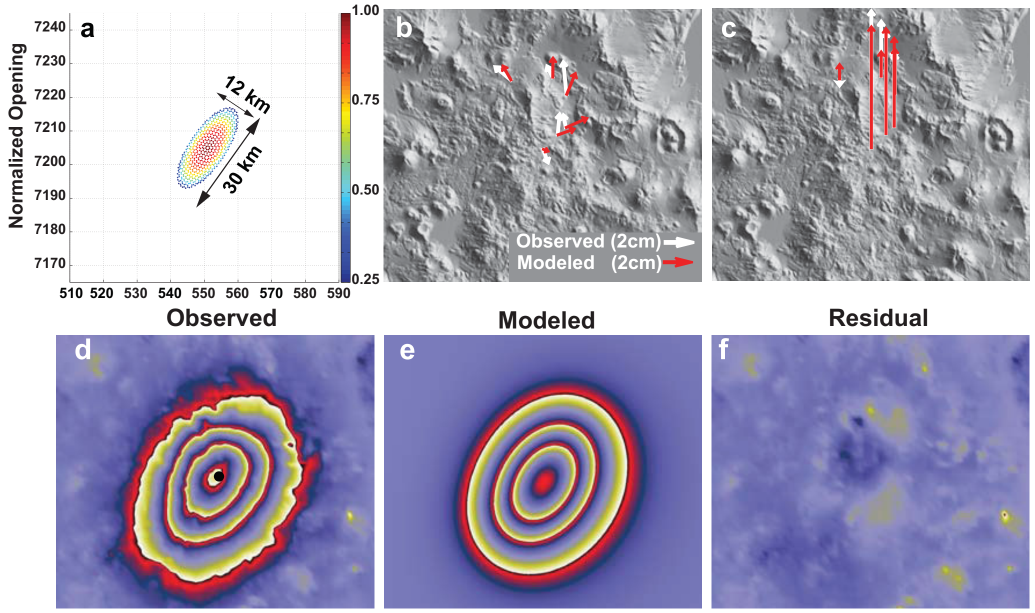

Descending track 282 orbit 34170 (6.13 years wrt 09/03/2003)

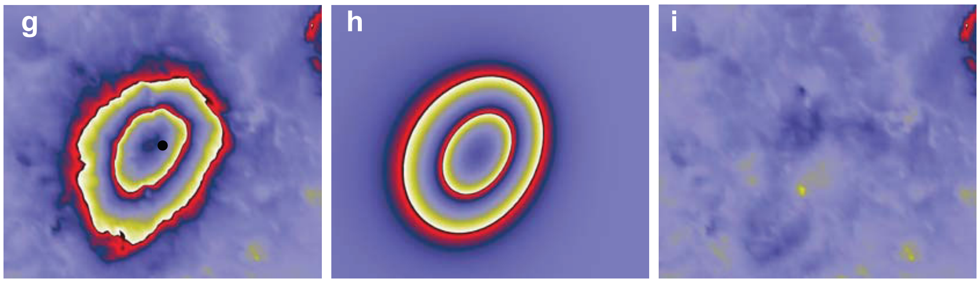

Ascending track 318 orbit 35493 (3.5 years wrt 03/08/2005)

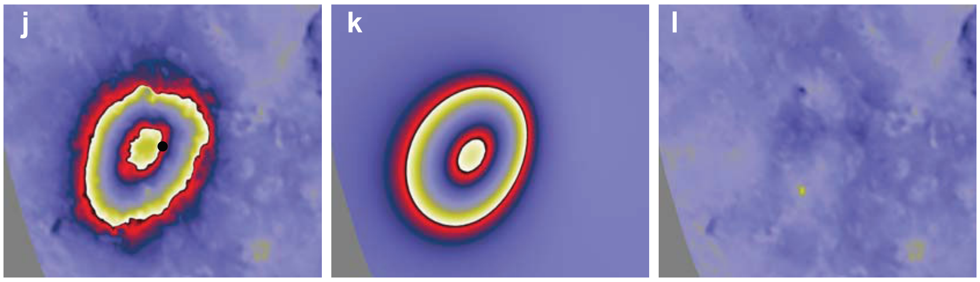

Ascending track 604 orbit 37031 (3.35 years wrt 22/11/2005)

**Figure 9.** Maps of observed and modeled GPS and InSAR data using the best elliptical crack model inferred by the inversion of InSAR and GPS data. (a) The best elliptical crack model with the normalized value of the opening. It is located at about 11 km depth and its dimensions are about 30 km and 13 km for the major and minor axes, respectively. (b) Horizontal GPS displacements (white vectors) for March 2006 to November 2008 and modeled displacement vectors (red vectors). (c) Vertical GPS displacements (white vectors) for March 2006 to November 2009 and modeled displacement (red vectors). The RMS of the residual between GPS and modeled data is about 1 cm. The largest discrepancies observed at LST5 and LST6 (horizontal component) might be explained by shorter duration time. (d–l) Three LOS displacements maps and the model predictions. (d, g, and j) Observed LOS displacement maps using the InSAR data subsampled to 500 m. (e, h, and k) Modeled data using the elliptical crack model. (f, i, and l) Residual between observed and modeled data. The RMS of the residuals ranges from 4 to 5 mm in these examples. The reduced $\chi^2_m$ of the residual for the whole data set is 0.78. The volume change rate is $14.8 \times 10^6$ m$^3$ yr$^{-1}$ inducing a pressure change rate of about $8 \times 10^{-2}$ MPa yr$^{-1}$ assuming a shear modulus of 30 GPa. The black circles show the location of the GPS station LST7.

**Table 5.** Resulting Elliptical Truncated Cone Model Parameters Inferred From the Inversion of the Geodetic Data[a]

| | | | 95% Confidence Intervals | | |
|---|---|---|---|---|---|
| Parameters | Minimum Values | Maximum Values | Lower | Upper | Best Values |
| X (km) | 549 | 554 | 550.720 | 553.380 | 552.380 |
| Y (km) | 7203 | 7208 | 7204.350 | 7207.350 | 7206.500 |
| Depth (m) | 1000 | 20,000 | 2010 | 13,890 | 5315 |
| Major axis (m) | 5000 | 40,000 | 12,400 | 36,000 | 26,540 |
| S2/S1 | 0.1 | 1 | 0.08 | 0.75 | 0.56 |
| DipS1 (°) | 15°S | 15°N | 12°S | 5°N | 2°S |
| DipS2 (°) | 15°W | 15°E | 8°W | 13°E | 1°E |
| Azimuth (°) | N80°E | N | N46°E | N18°E | N34°E |
| H (m) | 100 | 10,000 | 100 | 8900 | 5622 |
| $\alpha$ (°) | −80 | +80 | −80 | 80 | 50 |
| Volume (km$^3$)[b] | | | *1.60* | *5538* | *2769* |
| Roof area (km$^3$)[b] | | | *42* | *670* | *315* |

[a] X and Y are expressed in km (UTM WGS84 zone 19 South). Depth is expressed in m below the mean surface elevation (i.e., 4500 m a.s.l). S1 is the major axis. S2/S1 is the length ratio between the major and minor axes. DipS1 and DipS2 are the dip angles of the major axis (S1) and the minor axis (S2), respectively. H is the thickness of the source. Azimuth is a clockwise angle relative to the North. $\alpha$ is the dip angle of the source walls. $\alpha < 0$ means that the source walls dip outward, $\alpha > 0$ means the source walls dip inward.

[b] Confidence interval and best estimation for the source volume are estimated using the geometric parameters inferred by the inversion.

($\alpha \sim 50°$). The thickness is about 5 km, leading to an estimated source volume of 2769 km$^3$. The volume change rate is estimated at about $12.5 \times 10^6$ m$^3$ yr$^{-1}$ and the pressure change rate at about $2 \times 10^{-2}$ MPa yr$^{-1}$. The reduced $\chi^2_m$ of the residual between the values predicted by this model and the data is 0.78. The RMS of residuals for InSAR is about 4 mm while the corresponding RMS for the GPS is 10 mm showing that a large massive shallow source explains the geodetic time series at Lazufre as well as the crack type source. Figure 11 shows the displacements observed on the largest period of each track, the modeled displacements using the elliptical truncated cone model with the smallest misfit and their residuals.

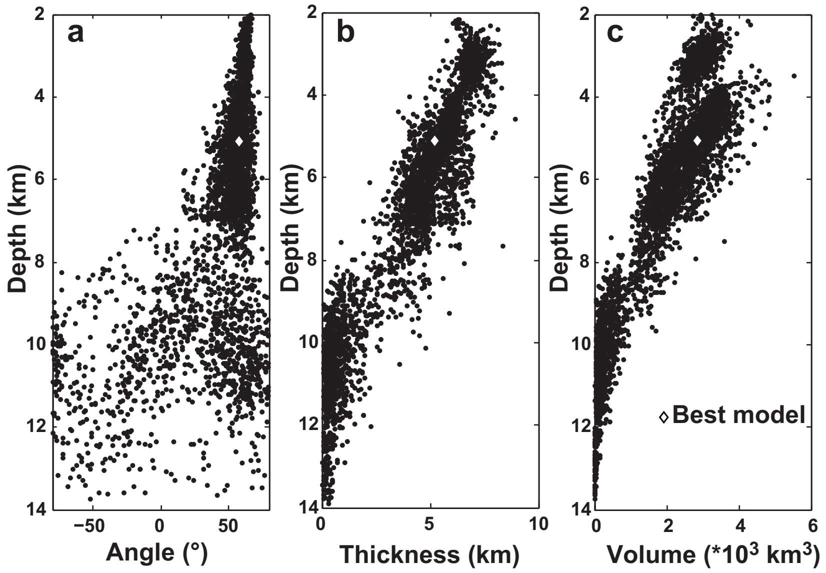

**Figure 10.** Dispersions of three model parameters versus the depth for the elliptical truncated cone model. Each black dot represents a model solution for a given pair of parameters that falls within the 95% confidence interval. White diamonds show the best model, with a reduced $\chi^2_m = 0.78$. (a) Scatter plot of dip angle of the walls versus depth. The minimum source depth of acceptable models is about 2000 m below the ground surface. The shallowest sources are characterized by outward dipping walls ($\alpha > 0$). Below a source depth of 8500 m the deformation data are completely insensitive to the dip angle. (b) Scatter plot of the thickness versus depth. There is a strong trade-off between these two parameters. For a given depth, the thickness uncertainty is generally large except for the shallowest or the deepest sources. (c) Scatter plot of the volume versus depth. The trade-off between these parameters leads to a strong high variation in the inferred volume, which ranges from 1.60 to 5500 km$^3$.

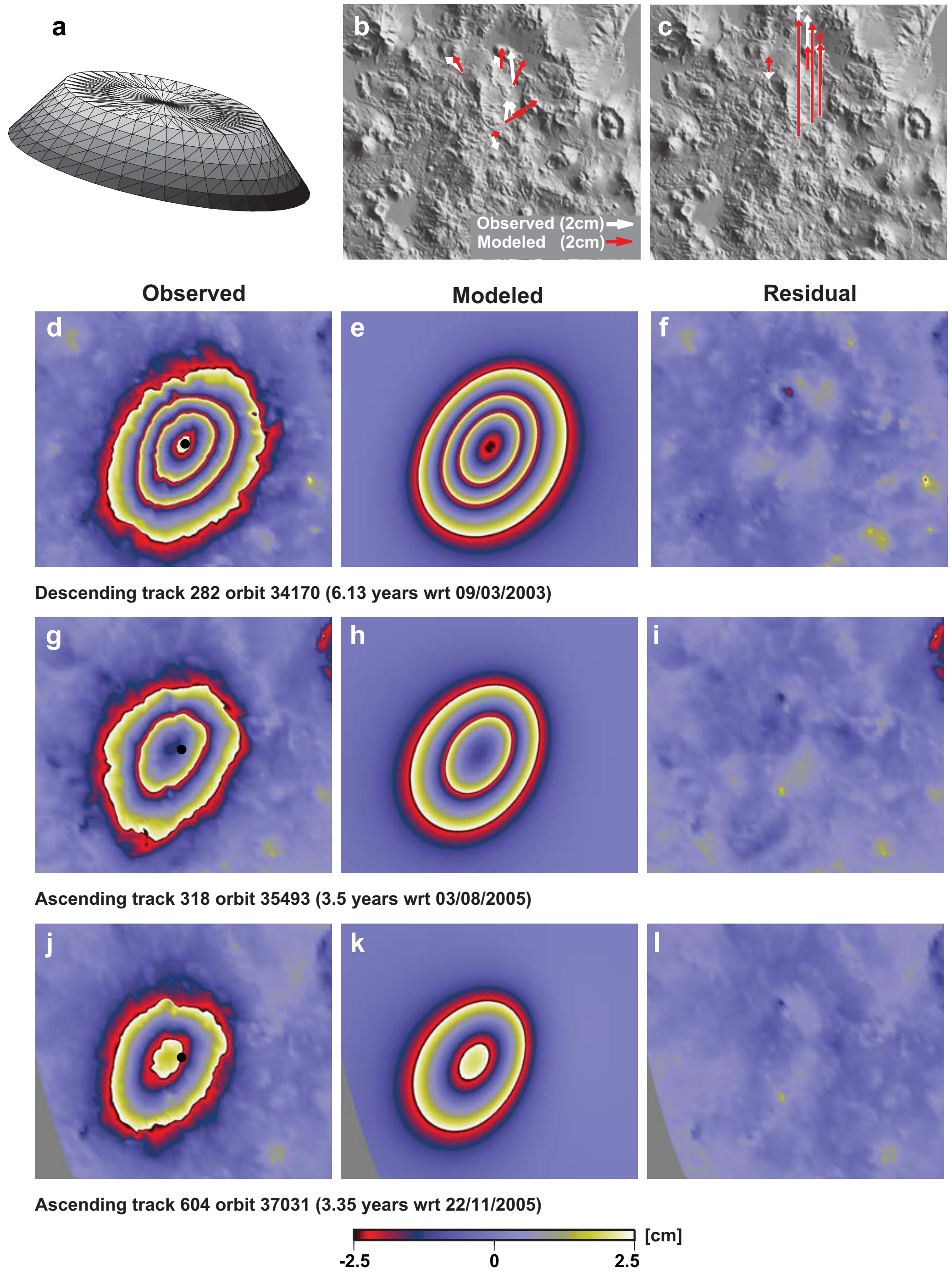

**Figure 11.** Maps of observed and modeled GPS and InSAR data using the elliptical truncated cone model. (a) Meshed truncated cone model used in this study. The better displacement source inferred by the inversion is located at about 5.3 km depth and its dimensions are about 27 km and 15 km for the major and minor axes, respectively. (b) Horizontal GPS displacements (white vectors) for March 2006 to November 2008 and modeled displacements vector (red vectors). (c) Vertical GPS displacements (white vectors) for March 2006 to November 2009 and modeled displacements (red vectors). The RMS of the residual between GPS and modeled data is about 1 cm. The largest discrepancies observed at LST5 and LST6 (horizontal component) might be explained by shorter duration time. (d–l) Example of three LOS displacements maps and the model prediction computed using the first component of the PCAIM decomposition. (d, g, and j) Observed LOS displacement maps using the InSAR data subsampled to 500 m. (e, h, and k) Modeled data using the elliptical truncated cone model with the first principal values and their corresponding time function value. (f, i, and l) Residual between observed and modeled data. The RMS of the residuals ranges from 4 to 5 mm in these examples. The $\chi_r^2$ of the residual for the whole data set is 0.78. The volume change rate is $12.5 \times 10^6$ m$^3$ yr$^{-1}$ leading to a pressure change rate of about $2 \times 10^{-2}$ MPa yr$^{-1}$ assuming a shear modulus of 30 GPa. The black circles show the location of the GPS station LST7.

## 6. Discussion and Conclusions

Two main types of source models have been proposed in previous studies to explain the surface displacement at Lazufre: (i) growing sources, propagating laterally at a rate of between 4 and 8 km yr$^{-1}$ [*Ruch et al.*, 2008; *Anderssohn et al.*, 2009] or (ii) preexisting sources in which the internal pressure increases without any major change in the source dimensions and location during the period of observation [*Pritchard and Simons*, 2002, 2004; *Froger et al.*, 2007; *Pearse and Lundgren*, 2013]. The large temporal coverage and improved sensitivity to source geometry provided by the geodetic data set we used in the present study provide better constrains both on the displacement source shape and on its temporal evolution, allowing us to eliminate the growing sources proposed by *Ruch et al*. [2008] and *Andersshon at al*. [2009]. We were also able to propose possible processes to explain the observed displacements.

The main results of our study can be summarized as follows:

1. The ground surface displacement at Lazufre continued at least until 2010, indicating a persistent uplift in this area for more than one decade, since it is assumed to have begun sometime between 1996 and 1998 [*Pritchard and Simons*, 2002, 2004].

2. The PCAIM analysis shows that the source shape and location did not change significantly during the period between spring 2003 and spring 2010. It also shows that, assuming the crust acts as an elastic medium, the internal pressure within the source increased with a remarkably constant rate over this period ($\sim$2–8 $\times$ 10$^{-2}$ MPa yr$^{-1}$).

3. The ground surface displacement pattern, drawn from the PCAIM analysis, exhibits a clear elliptical shape. This suggests a source with a marked ellipticity and thus rules out the axisymmetric source models often used in previous studies (i.e., spheres, horizontal penny-shaped sources, prolate, or oblate spheroids with rotational axes close to vertical) [*Pritchard and Simons*, 2002, 2004; *Froger et al*., 2007].

4. Assuming that the source is embedded in an elastic half-space, the comparison of the EW and vertical components of displacement strongly suggests a flat-topped source. It should be noticed that domed sources not only produce higher maximum horizontal displacement to maximum vertical displacement ratios than flat-topped sources but they also require a more marked ellipticity of shape, in the horizontal plane, to produce the same elliptical pattern of displacement at the surface.

5. Inversions carried out for two source types (elliptical crack and truncated elliptical cone) give very close results for the center location, the orientation and the dip of the surface displacement source. The center of the source is located 11.5 km SSE from Lastarria and 9.5 km NNE from Cordon del Azufre, i.e., slightly to the east (6 km) of the Lazufre Quaternary volcanic chain axis (Figure 1). The best sources dip slightly down to the east and its major axis is elongated N34°E–35°E, one of the main structural directions in the area [*Riller et al*., 2006], suggesting a possible structural control on the source location and geometry.

6. Depths of source roof, below ground surface, range from 8700 to 14,000 m, and from 2000 to 13,800 m, for best elliptical crack models and best truncated elliptical cone models, respectively (at 95% confidence level). As displacements at the surface of crack models, with low dip angle, are mostly vertical, only the deepest ($>\sim$8000 m) can produce significant horizontal displacements at the ground surface, close to the observed ones. This constraint does not affect truncated elliptical cone models in the same way since, for the shallowest ones, horizontal ground displacements can be obtained by having source walls dipping outward. On the other hand there is an obvious positive trade-off between depth and major axis length of truncated cone, whereas there is a negative trade-off between depth and thickness for this type of source. Truncated cones with roof shallower than $\sim$8000 m have walls dipping outward. For deeper sources, the signal appears insensitive to the wall dip. These results suggest that, at first order, a continuum of acceptable models exists from thick sources ($H \approx 7000$ m) with a shallow (depth $\approx$ 2000 m) and relatively small ($S1 \approx 15{,}000$ m) roof and walls dipping outward with low dip angles ($\sim$60° from vertical), to thin (either truncated cones with $H \leq 100$ m or elliptical cracks) deep (9000 m $\leq$ depth $\leq$ 14,000 m) sources with large roof ($S1 \approx 35{,}000$ m). For these deep sources, the dip of their walls has no significant influence on the signal and can vary from 80° outward to 80° inward (cf. Figure 10a). Thus, even if the inversions do not provide very good constraints on the model depth, the range of acceptable values (2000–14,000 m) clearly suggests a source within the upper crust. In addition, preliminary results of a study based on seismic noise correlation [*Spica et al*., 2012] suggest that the source may be deeper than 7 km.

7. The volume estimate for the truncated elliptical cone model lying at shallow depth (<8000 m) might seem large (greater than 400 km$^3$, Figure 10c) but it is plausible in view of the volume of some ignimbrites emitted in the vicinity of Lazufre. The Cerro Galan caldera, for instance, is the source of a ~1000 km$^3$ ignimbrite [*Francis et al.*, 1983] and La Pacana caldera is the source of at least two major ignimbrite eruptions with a combined estimated volume of some 2700 km$^3$ [*Lindsay et al.*, 2001].

8. The estimated rate of volume change, whatever the source type, is about $12.5 \times 10^6 - 14.8 \times 10^6$ m$^3$ yr$^{-1}$. This range is fully compatible with the peak intrusion rates proposed by *De Silva and Gosnold* [2007] for the building of upper crustal plutons associated with the Neogene volcanic activity of APVC. It is also compatible with the instantaneous intrusion rates proposed by *De Saint Blanquat et al*. [2006] for the Black Mesa pluton. On other volcanic regions, an increase (or decrease) of pressure in a sealed geothermal reservoir is invoked to explain uplift or subsidence in large caldera settings such as Yellowstone, Long Valley or Campi Flegrei [*Wicks et al*., 1998; *Dzurisin et al*., 1999; *Fialko et al*., 2001b]. Nevertheless, at Lazufre there is not clear evidence of a large caldera depression than can serve as structural trap for a geothermal system and surface manifestations classically associated with a geothermal field have not been reported at Lazufre [*De Silva and Francis*, 1991; *Pritchard and Simons*, 2002].

Our results show that the surface displacement measured at Lazufre can be explained without any need for significant lateral source expansion, as proposed by *Ruch et al*. [2008] and *Andersshon at al*. [2009]. The apparent grow of the displacement pattern with time can easily be explained by the expanding emergence of the signal from background noise as its amplitude increases. Moreover, the changes in the source shape, obtained by *Andersshon at al*. [2009], for the different epochs of its InSAR time series, may actually result from the modeling of undesirable transient components in their displacement signal (e.g., insufficiently corrected atmospheric component). Instead of an expanding source, we favor a preexisting source for which the location, the shape, and the dimensions do not change, but in which the internal pressure increases linearly with time. It is worth mentioning that [*Pearse and Lundgren*, 2013], using an approach that was different from the one used in this study, reached to the same conclusion.

In order to further explain the process at the origin of the Lazufre surface displacement, it is worth comparing the Lazufre signal with another large uplift, located in Bolivia, less that 400 km to the northeast of Lazufre and centered on the Uturuncu volcano. Both the Lazufre and Uturuncu have shown uninterrupted large-wavelength uplift activity for more than 10 years and with remarkably constant displacement rate. They are both interpreted as being related to magmatic activity in depth. On the other hand, the two signals differ in some aspects: the displacement pattern at Uturuncu is axisymmetric, while the one at Lazufre is elliptical, and the displacement pattern at Uturuncu has a larger wavelength but a lower rate [~1–2 cm yr$^{-1}$, *Pritchard and Simons*, 2002; *Sparks et al*., 2008] than the one at Lazufre (~3 cm yr$^{-1}$).

Moreover, from a new InSAR data set, extended in time with respect to the one used by *Pritchard and Simons* [2002], *Fialko and Pearse* [2012] detected a low amplitude large-wavelength peripheral subsidence surrounding the Uturuncu uplift, later confirmed by *Henderson and Pritchard*, [2013]. A peripheral subsidence like this, combined with a central uplift, seems to indicate a mass transfer either from a deep area to a shallower one or from a peripheral area to a more central one (or possibly a combination of the two). Peripheral subsidence has not been observed at Lazufre, although this does not necessarily mean that there was no mass transfer here. At very low subsidence rates, as at Uturuncu, the time span for the available InSAR data at Lazufre might not be long enough to allow such a subtle signal to be deciphered from background noise.

Another important difference between the two surface displacements is that all the models indicate a deeper source at Uturuncu (between 18 and 35 km below the surface [*Pritchard and Simons*, 2002; *Fialko and Pearse*, 2012; *Hickey et al*., 2013] than at Lazufre, where the source is clearly located within the upper crust [between 2 and 18 km below the surface, *Pritchard and Simons*, 2004; *Froger et al*., 2007; *Ruch et al*., 2008; *Anderssohn et al*., 2009; *Henderson and Pritchard*, 2013; *Pearse and Lundgren*, 2013]. Taking the results of InSAR data modeling into account, as well as those provided by other geophysical data as well as geological, geochronology, petrological, and geochemical data, it has been proposed that the source of the Uturuncu surface displacement is closely related to the Altiplano-Puna Magma Body (APMB) [*Sparks et al*., 2008; *Fialko and Pearse*, 2012; *Hickey et al*., 2013]. The APMB is a large midcrustal zone of partial melting considered as the source of the Altiplano Puna Volcanic Complex [*De Silva*, 1989; *De Silva and Gosnold*, 2007]. First inferred from petrological arguments [*De Silva*, 1989] the presence of an extensive partial melt layer beneath the southern Altiplano and Puna was later confirmed by seismic data that indicated the presence of a ~2 km thick very-low-velocity layer at depth of 17 and 19 km [*Chmielowski et al*., 1999; *Leidig and Zandt*, 2003; *Zandt et al*., 2003]. From electrical conductivity data, *Schilling et al*. [2006] evaluate that the interconnected melt network, within the APMB, represents about 20% of the total volume. *De Silva and Gosnold* [2007] proposed that the dacitic magmas, derived from fractionation of the APMB melt phase, percolated intermittently into the upper crust. They also demonstrated that the presence of the APMB has produced a significant and progressive perturbation of the crustal geotherm, resulting in a rise of the brittle-ductile-transition zone (BDTZ) to a shallow depth. In their model, the BDTZ represents a major mechanical discontinuity in the crust that may have trapped the dacitic magmas rising from APMB. As a result, the magmas accumulated at depths of between 4 and 8 km to form large shallow magma chambers that were later the sources of the ignimbritic eruptions of the APVC. The modalities of magma migration from APMB to BDTZ are still debated (diffuse percolation, brief and voluminous intrusion, diapirism, etc.). The different interpretations proposed for the Uturuncu surface displacement mirror this debate. For *Fialko and Pearse* [2012], the Uturuncu uplift manifests the rising of a large diapir from the roof of the APMB. *Hickey et al*. [2013] favor instead a static model of a magmatic body rooted in the APMB, but with increasing internal pressure. This last model, however does not account for the peripheral subsidence.

The Lazufre surface displacement cannot be explained, in the same way as Uturuncu surface displacement, as being directly caused by a process at the level of an APMB-like partially melted layer. On the one hand, there is no clear evidence of a wide partially melted zone, similar to APMB beneath the Lazufre area and, on the other hand, all the models support a source located at a shallower level in the upper crust [*Pritchard and Simons*, 2002, 2004; *Froger et al*., 2007; *Ruch et al*., 2008; *Anderssohn et al*., 2009; *Henderson and Pritchard*, 2013; *Pearse and Lundgren*, 2013]. Instead of a wide partially melted zone, *Budach et al*. [2013], on the base of magnetotelluric data, proposed than melts ascent from the upper mantle through a narrower structure (some tens of km wide) and fed a potential magma reservoir within the upper crust, beneath Lazufre volcanic center.

Both the Lazufre and Uturuncu surface displacements exhibit a remarkably linear time dependency. To account for that characteristic at Uturuncu, both *Fialko and Pearse* [2012] and *Hickey et al*. [2013] employed a viscoelastic rheology for the crust surrounding the surface displacement source (although they have chosen drastically different viscoelastic models). A viscoelastic rheology does indeed appear relevant considering the supposed depth of the Uturuncu surface displacement source (>18 km).

In this study, we have initially made the assumption that the surface displacement source is embedded in an elastic medium. The range of depths we have obtained for the best source models as well as the depths obtained in previous studies [*Pritchard and Simons*, 2004; *Froger et al*., 2007; *Ruch et al*., 2008; *Anderssohn et al*., 2009; *Henderson and Pritchard*, 2013; *Pearse and Lundgren*, 2013] are compatible with this assumption. The linearity of internal pressure increase within the source, however, is more difficult to explain in a strictly elastic context. It would require that the process at the origin of the displacements is a constant rate process, which has remained constant from 1996–1998 to now. A continuous supply of magma ascending the mantle at a constant rate for more than one decade would require a constant magma production rate and a steadiness of the magma pathway through the crust. A more likely explanation could be that a brief initial input of magma within the source induced a continuous rate of pressure increase due to the progressive oversaturation of volatile species released by fractional crystallization.

However, we cannot discard the hypothesis that the apparent linear time dependency of surface displacement observed at Lazufre could be explained by a viscoelastic relaxation mechanism. *Newman et al*. [2006] and *Del Negro et al*. [2008] showed that a transient or intermittent increase of pressure in a magma chamber could produce displacements that are smoothed and delayed over time in such a way that the apparent displacement rate appears constant. Such a mechanism has also been proposed to explain the remarkable linear rate of surface displacement observed in Socorro, New Mexico, for more than 100 years [*Fialko and Simons*, 2001; *Fialko et al*., 2001b; *Pearse and Fialko*, 2010]. Two main effects could be invoked to explain a viscoelastic relaxation mechanism induced by a reduction of viscosity in the crust surrounding the surface displacement source. First, the presence of a partially melted structure beneath the Lazufre area, as evidenced by *Budach et al*. [2013] may have resulted in a progressive thermal softening of the overlying crust. Second, if the growth of the magmatic body responsible for the Lazufre surface displacement began sufficiently long ago, one can assume that the surrounding rocks would have been heated and weakened beyond the brittle-ductile transition temperature to behave in a viscoelastical manner, as it has been proposed for the Long Valley Caldera magmatic body by *Newman et al*. [2006].

In addition to these two effects, one can also invoke viscoelastic relaxation processes occurring within the source itself. If the source is a magmatic body that grew incrementally by accretion from bellow of successive sills, as it has been proposed by *De Saint Blanquat et al*. [2006] for the Black Mesa pluton, for instance, one can hypothesize that the $n - 1$ previously emplaced sills, depending on their respective thermal state, will globally behave like a viscous blanket that will reduce the displacements induced by the nth sill intrusion over time. Moreover, this pile of $n - 1$ emplaced sills could also filter the displacement in space so that the final shape of surface displacement pattern will not reflect the shape of the last sill intruded, at the bottom of the pile, but rather the shape of the oldest one at the top of the pile.

Obviously, a rigorous evaluation of these different viscoelastic processes, as possible candidates to explain the Lazufre surface displacement spatiotemporal evolution, is not possible until the rheological properties of the crust in this area of the southern CVZ are better constrained. For this purpose, a large and dense seismic tomography survey would be the next step to go further in our understanding of the Lazufre surface displacement.

**Acknowledgments**
The authors would like to especially thank Fran Van Wyk de Vries for proofreading an early version of this manuscript. ENVISAT data are acquired through ESA-ENVISAT-AO project 857 and ESA category 1 research project 2899. The GPS surveys have been carried out with logistic support of Representation IRD in Chile and Universidad de Chile. This research is supported by IRD, UMR 5563 (GET Toulouse), and UMR 6524 (LMV Clermont-Ferrand). Some of the figures in this paper were made using Generic Mapping Tools (GMT) [*Wessel and Smith*, 1991]. Insightful reviews by two anonymous reviewers greatly improved this paper.

## References

Aguilera, F., F. Tassi, T. Darrah, S. Moune, and O. Vaselli (2012), Geochimical model of magmatic-hydrothermal system at Lastarria volcano, northern Chile, *Bull. Volcanol.*, *79*, 119–134.

Anderssohn, J., M. Motagh, T. R. Walter, M. Rosenau, H. Kaufmann, and O. Oncken (2009), Surface deformation time series and source modeling for a volcanic complex system based on satellite wide swath and image mode interferometry: The Lazufre system, central Andes, *Remote Sens. Environ.*, *113*(10), 2062–2075.

Bonvalot, S., D. Remy, J. Froger, G. Gabalda, P. Labazuy, D. Legrand, F. Aguillera, F. Bondoux, and M. De Saint Blanquat (2008), Present-day magmatic pulses in the Andes? Results from geodesy and geophysics, *Geophys. Res. Abstr.*, *10*, EGU2008–A-08675.

Budach, I., H. Brasse, and D. Daz (2013), Crustal-scale electrical conductivity anomaly beneath inflating Lazufre volcanic complex, Central Andes, *J. South Am. Earth Sci.*, *42*, 144–149.

Cayol, V., and F. H. Cornet (1998), Effects of topography on the interpretation of the deformation field prominent volcanoes: Application to Etna, *Geophys. Res. Lett.*, *25*, 1979–1982.

Chen, C. W., and H. A. Zebker (2002), Phase unwrapping for large SAR interferograms: Statistical segmentation and generalized network models, *IEEE Trans. Geosci. Remote Sens.*, *40*, 1709–1719.

Chmielowski, J., G. Zandt, and C. Haberland (1999), The Central Andean Altiplano-Puna Magma Body, *Geophys. Res. Lett.*, *26*, 783–786.

CNES/Altamira-information (1996), Philosophie et mode d'emploi de la chaîne logicielle interférométrique DIAPASON, Toulouse, France.

De Saint Blanquat, M., G. Habert, E. Horsman, S. S. Morgan, B. Tikoff, P. Launeau, and G. Gleizes (2006), Mechanisms and duration of non-tectonically assisted magma emplacement in the upper crust: The Black Mesa pluton, Henry Mountains, Utah, *Tectonophysics*, *428*, 1–31.

De Silva, S. L. (1989), Altiplano-Puna volcanic complex of the central Ande, *Geology*, *17*, 1102–1106.

De Silva, S. L., and P. W. Francis (1991), *Volcanoes of the Central Andes*, 232 pp., Springer, Heidelberg.

De Silva, S. L., and W. D. Gosnold (2007), Episodic construction of batholiths: Insights from the spatiotemporal development of an ignimbrite flare-up, *J. Volcanol. Geotherm. Res.*, *167*(1–4), 320–335.

Del Negro, C., G. Currenti, and D. Scandura (2008), Temperature-dependent viscoelastic modeling of ground deformation: Application to Etna volcano during the 1993–1997 inflation period, *Phys. Earth Planet. Inter.*, *172*(3–4), 299–309, doi:10.1016/j.pepi.2008.1010.1019.

Dieterich, J. H., and R. W. Decker (1975), Finite element modelling of surface deformation associated with volcanism, *J. Geophys. Res.*, *80*, 4094–4102.

Dzurisin, D., C. Wicks, and W. Thatcher (1999), Renewed uplift at the Yellowstone Caldera measured by levelling surveys and satellite radar interferometry, *Bull. Volcanol.*, *61*, 349–355.

Fialko, Y., and M. Simons (2001), Evidence for on-going inflation of the Socorro magma body, New Mexico, from Interferometric Synthetic Aperture Radar imaging, *Geophys. Res. Lett.*, *28*, 3549–3552.

Fialko, Y., and J. Pearse (2012), Sombrero uplift above the Altiplano-Puna Magma Body: Evidence of a ballooning mid-crustal diapir, *Science*, *338*(6104), 250–252.

Fialko, Y., Y. Khazan, and M. Simons (2001a), Deformation due to a pressurized horizontal circular crack in an elastic half-space, with applications to volcano geodesy, *Geophys. J. Int.*, *146*, 181–190.

Fialko, Y., M. Simons, and Y. Khazan (2001b), Finite source modelling of magmatic unrest in Socorro, New Mexico and long Valley, California, *Geophys. J. Int.*, *146*, 191–200.

Francis, P. W., L. O'Callaghan, G. A. Kretzschmar, R. S. Thorpe, R. S. J. Sparks, R. N. Page, R. E. de Barrio, G. Gillou, and O. E. Gonzalez (1983), The Cerro Galan ignimbrite, *Nature*, *301*(5895), 51–53.

Froger, J. L., D. Remy, S. Bonvalot, and D. Legrand (2007), Two scales of inflation at Lastarria-Cordon del Azufre volcanic complex, central Andes, revealed from ASAR-ENVISAT interferometric data, *Earth Planet. Sci. Lett.*, *255*(1–2), 148–163, doi:10.1016/j.epsl.2006.12.012.

Fukushima, Y., V. Cayol, and P. Durand (2005), Finding realistic dyke models from INSAR data: The February 2000 eruption at Piton de la Fournaise, *J. Geophys. Res.*, *110*, B03206, doi:10.1029/2004JB003268.

Henderson, S. T., and M. E. Pritchard (2013), Decadal volcanic deformation in the Central Andes Volcanic Zone revealed by InSAR time series, *Geochem. Geophys. Geosyst.*, *14*, 1358–1374, doi:10.1002/ggge.20074.

Herring, T. A., R. W. King, and S. C. McClusky (2010), *Introduction to GAMIT/GLOBK, Release 10.4*, technical report., Dep. of Earth, Atmos., and Planet. Sci., pp. 1–47, Massachusetts Inst. of Technol., Cambridge, Mass.

Hickey, J., J. Gottsmann, and T. Del Potro (2013), The large-scale surface uplift in the Altiplano-Puna region of Bolivia: A parametric study of source characteristics and crustal rheology using finite element analysis, *Geochem. Geophys. Geosyst.*, *14*, 540–555, doi:10.1002/ggge.20057.

Kositsky, A. P., and J.-P. Avouac (2010), Inverting geodetic time series with a principal component analysis-based inversion method, *J. Geophys. Res.*, *115*, B03401, doi:10.1029/2009JB006535.

Leidig, M., and G. Zandt (2003), Modeling of highly anisotropic crust and application to the Altiplano-Puna volcanic complex of the central Andes, *J. Geophys. Res.*, *108*(B1), 2014, doi:10.1029/2001JB000649.

Lin, Y.-N., A. P. Kositsky, and J.-P. Avouac (2010), PCAIM joint inversion of InSAR and ground-based geodetic time series: Application to monitoring magmatic inflation beneath the Long Valley Caldera, *Geophys. Res. Lett.*, *37*, L23301, doi:10.1029/2010GL045769.

Lindsay, J. M., A. K. Schmitt, R. B. Trumbull, S. L. De Silva, W. Siebel, and R. Emmermann (2001), Magmatic evolution of the La Pacana Caldera System, Central Andean CVZ, Chile: Compositional variation of two cogenetic, large-volume felsic ignimbrites, *J. Petrol.*, *42*(3), 459–486.

Massonnet, D., and K. L. Feigl (1998), Radar interferometry and its application to changes in the Earth's surface, *Rev. Geophys.*, *36*, 441–500.

Mogi, K. (1958), Relations between the eruptions of various volcanoes and the deformation of the ground surface around them, *Bull. Earthquake Res. Inst. Univ. Tokyo*, *36*, 99–134.

Newman, A. V., T. H. Dixon, and N. Gourmelen (2006), A four-dimensional viscoelastic deformation model for Long Valley Caldera, California, between 1995 and 2000, *J. Volcanol. Geotherm. Res.*, *150*, 244–269.

Okada, Y. (1992), Internal deformation due to shear and tensile faults in a half-space, *Bull. Seismol. Soc. Am.*, *82*(2), 1018–1040.

Pearse, J., and Y. Fialko (2010), Mechanics of active magmatic intraplating in the Rio Grande Rift near Socorro, New Mexico, *J. Geophys. Res.*, *115*, B07413, doi:10.1029/2009JB006592.

Pearse, J., and P. Lundgren (2013), Source model of deformation at Lazufre volcanic center, central Andes, constrained by InSAR time series, *Geophys. Res. Lett.*, *40*, 1059–1064, doi:10.1002/grl.50276.

Perfettini, H., et al. (2010), Seismic and aseismic slip on the Central Peru megathrust, *Nature*, *465*(7294), 78–81.

Pritchard, M. E., and M. Simons (2002), A satellite geodetic survey of large scale deformation of volcanic centres in the central Andes, *Nature*, *418*, 167–170.

Pritchard, M. E., and M. Simons (2004), An InSAR-based survey of volcanic deformation in the central Andes, *Geochem. Geophys. Geosyst.*, *5*, Q02002, doi:10.1029/2003GC000610.

Riller, U., H.-J. Götze, S. Schmidt, R. Trumbull, F. Hongn, I. Petrinovic (2006), Upper-crustal structure of the central Andes inferred from dip curvature analysis of isostatic residual gravity, in edited by O. Oncken, G. Chong, G. Franz, et al., pp. 327–336, *The Andes - Active Subduction Orogeny*, (Frontiers in Earth Sciences), Springer.

Ruch, J., J. Anderssohn, T. R. Walter, and M. Motagh (2008), Caldera-scale inflation of the Lazufre volcanic area, South America: Evidence from InSAR, *J. Volcanol. Geotherm. Res.*, *174*(4), 337–344.

Ruch, J., A. Manconi, G. Zeni, G. Solaro, A. Pepe, M. Shirzaei, T. R. Walter, and R. Lanari (2009), Stress transfer in the Lazufre volcanic area, central Andes, *Geophys. Res. Lett.*, *36*, L22303, doi:10.1029/2009GL041276.

Sambridge, M. (1999a), Geophysical inversion with a neighbourhood algorithm. II: Searching a parameter space, *Geophys. J. Int.*, *138*, 479–494.

Sambridge, M. (1999b), Geophysical inversion with a neighbourhood algorithm. I: Appraising the ensemble, *Geophys. J. Int.*, *138*, 727–746.

Schilling, F. R. et al. (2006), Partial Melting in the Central Andean Crust: a Review of Geophysical, Petrophysical, and Petrologic Evidence, in edited by O. Oncken, G. Chong, G. Franz, et al., pp. 459–474, *The Andes - Active Subduction Orogeny*, (Frontiers in Earth Sciences), Springer.

Sparks, R. S. J., C. B. Folkes, M. C. S. Humphreys, D. N. Barford, J. Clavero, M. C. Sunagua, S. R. McNutt, and M. E. Pritchard (2008), Uturuncu volcano Bolivia: Volcanic unrest due mid-crustal magma intrusion, *Am. J. Sci.*, *308*(6), 727–769.

Spica, Z., D. Legrand, A. Mendoza, D. Torsten, T. Walter, S. Hiemann, J. Froger, and D. Remy (2012), Surface waves calculated from seismic noise and very shallow seismicity of the Lastarria Volcanic Anomaly, Chile, paper presented at Reunión Anual 2012 de la Unión Geofísica Mexicana, Puerto Vallarta, Mexico, November.

Usai, S. (2003), A least squares database approach for SAR interferometric data, *IEEE Trans. Geosci. Remote Sens.*, *41*(4), 753–760.

Wessel, P., and W. H. F. Smith (1991), Free software help map and display data, *EOS Trans. AGU*, *72*, 441–446.

Wicks, C., W. Thatcher, and D. Dzurisin (1998), Migration of fluid beneath Yellowstone caldera inferred from satellite radar interferometry, *Science*, *282*, 458–462.

Wright, T., B. Parson, and L. Zhong (2004), Toward mapping surface deformation in three dimension using InSAR, *Geophys. Res. Lett.*, *31*, L01607, doi:10.1029/2003GL018827.

Yang, X.-M., and P. M. Davis (1988), Deformation from inflation of a dipping finite prolate spheroid in an elastic half-space as a model for volcanic stressing, *J. Geophys. Res.*, *93*, 4249–4257.

Yun, S., P. Segall, and H. Zebker (2006), Constraints on magma chamber geometry at Sierra Negra Volcano, Galápagos Islands, based on InSAR observations, *J. Volcanol. Geotherm. Res.*, *150*(1–3), 232–243.

Zandt, G., M. leidig, D. Chmielowsky, D. Beaumont, and X. Yuan (2003), Seismic detection and characterization of the Altiplano-Puna magma body, central Andes, *Pure Appl. Geophys.*, *160*, 789–807.